Mössbauer Effect Reference and Data Journal

April • Volume 47 • Number 02

Design of Novel Fe(II) Colorimetric Sensors for Detection of Volatile Organic Compounds

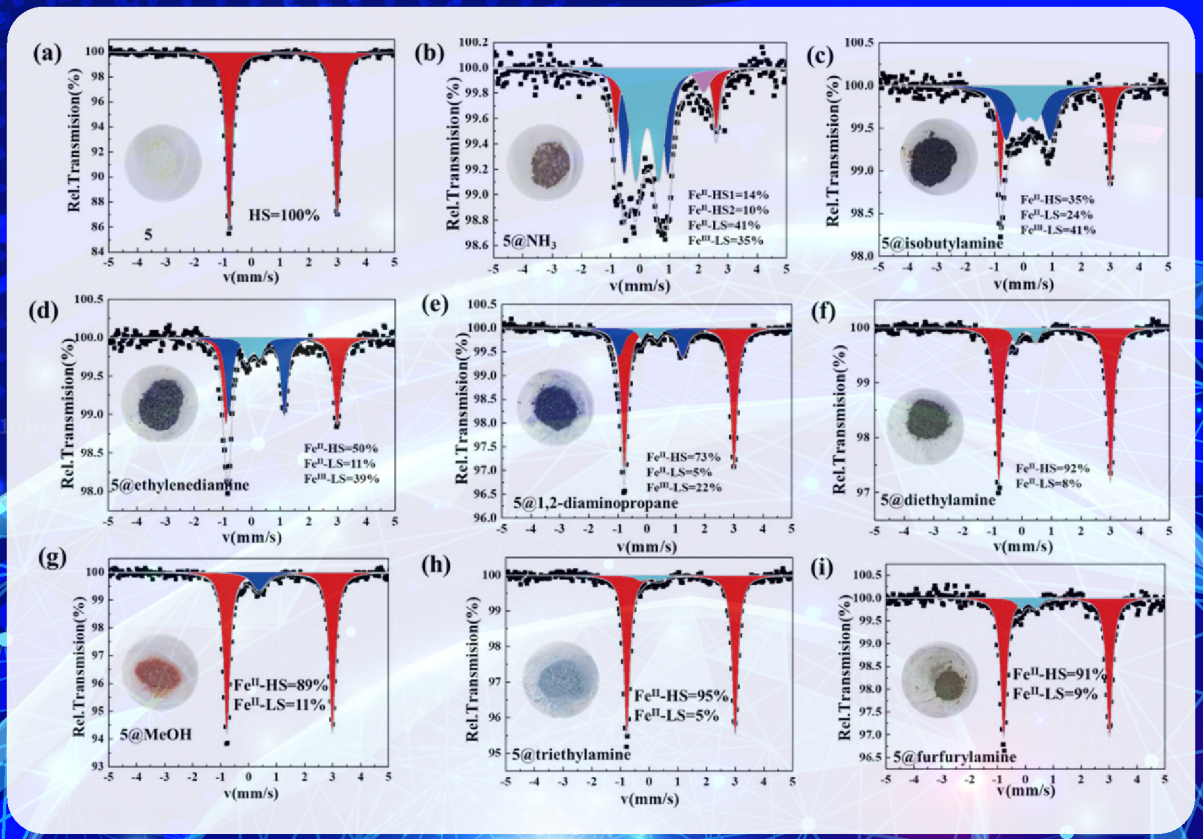

Mössbauer Effect Reference and Data Journal

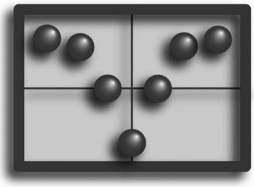

The *Mössbauer Effect Reference and Data Journal (MERDJ)* is published ten times a year (each month excluding January and February) plus an Index Issue at the end of December by the Mössbauer Effect Data Center.

Subscriptions: The annual subscription rate for Volume 47 (2024) is US$1,500.00 ($1,200.00 without the Index Issue). Subscription inquiries and address changes should be addressed to the General Manager at the address below.

Mössbauer Effect Data Center
Dalian Institute of Chemical Physics
Chinese Academy of Sciences
457 Zhongshan Road, Dalian
116023, China

Tel: +86 411 8437 9407
Email: medc@dicp.ac.cn
Web: www.medc.dicp.ac.cn

ISSN 0163-9587

On the cover:
This issue our front cover is focusing on the research work of Ms. Li Sun, a young Mössbauer spectroscopists from Prof. Yann Garcia's group at UCLouvain in Belgium. They designed a novel Fe(II) colorimetric sensor detection system in food chemistry (See more in Editor's Comments and in the enclosed Mössbauer Spectroscopy Newsletter.)

Mössbauer Effect Reference and Data Journal

April 2024 • Volume 47 • Number 2

Contents

Editor's Comments

Design of Novel Fe(II) Colorimetric Sensors for Detection of Volatile Organic Compounds

Nowadays, food quality and nutrition have rapidly become a case of social concern with the development of bio-products, eco food ad so on. Food chemistry can play a pivotal role in the understanding of contaminants formation and/or detection using advanced analytical chemistry tools. In this frame, this is no surprise that the European union recently launched a COST networking action on the study of acrylamide and asparagine contamination in bread and potatoes product, called ACRYRED.

This month, we highlight the work of a young Mössbauer spectroscopist, **Li Sun**, who recently was awarded the PhD degree in food chemistry after a dissertation written at Université catholique de Louvain, Belgium. The Mössbauer Effect Reference Data Journal wishes to encourage indeed early stage researchers (ESRs) and recently awarded PhD doctors to submit a summary of their thesis to the journal. These scientists form the next generation of spectroscopists which will animate our community in the future. Knowing better their work will allow not only allow them to establish networking contacts among the community but also to generate future opportunities and stimulate new research ideas and concepts.

Dr. **Li Sun**, who was educated in China and in Belgium (Louvain-la-Neuve), returned to her home country for a postdoctoral position at Ningbo Institute of Materials Technology &. Engineering in Ningbo to develop new nanomaterials for applications in bio sensing and environmental sciences.

Yann Garcia
Associate Editor
Institute of Condensed Matter and Nanosciences
Université Catholique de Louvain, Belgium

Mössbauer Effect Data Center

is pleased to offer these publications and services to the international Mössbauer community...

Mössbauer Effect Reference and Data Journal

The *Journal* reports as thoroughly as possible all published information on Mössbauer spectroscopy. An annual subscription includes ten issues plus an index issue. Each issue includes a Reference Listing, a Data Listing, an Isotope Index, a Subject Index, and the *Mössbauer Spectroscopy Newsletter*.

Mössbauer Web Sites
ON THE WORLD WIDE WEB

The Mössbauer Effect Data Center developed and administers two separate Web sites for the Mössbauer community (<www.moss.dicp.ac.cn> and <www.medc.dicp.ac.cn>). These sites provide Mössbauer researchers with pertinent and timely information, free of charge. Included on the sites are general information pertinent to the Mössbauer community, news items, regional lab information, position postings, information on upcoming conferences, the most recent *Mössbauer Spectroscopy Newsletter*, IBAME information, an E-Mail and Fax Directory of Mössbauer Authors, links to Mössbauer instrument and source suppliers, and further information regarding the Center's products and services. Access to the MEDC Web-Access Database is also provided through the MEDC site. Researchers may now access and search the MEDC database *from their computers* via the MEDC Web site.

For further information about these and our many other publications and services for the Mössbauer community, please visit us at our Web site

Dalian Institute of Chemical Physics
Chinese Academy of Sciences
457 Zhongshan Road, Dalian 116023, China
Phone: +86-411-84379159
Fax: +86-411-84685940
Email: medc@dicp.ac.cn
Web: www.medc.dicp.ac.cn www.moss.dicp.ac.cn

Code	Reference
23A040	H.H.An, C.S.Kim, J.H.Moon, N.S.Lee, and S.B.Kim*, *J. Radioanal. Nucl. Chem.* **332**(12),5127-33(2023) Mössbauer study of AFe_2O_4 (A=Mn, Fe, and Co) nanoparticles for biomedical applications.
23A041	V.Z.Abdrakhimov, *Coke Chem. (N. Y., NY, U. S.)* **66**(12),630-7(2023) Iron oxides and their composition in ceramic brick based on power plant waste: data from Mössbauer spectroscopy.
23A042	N.Amini, S.Habibi*, and N.Mohammadiparsa, *Glass Phys. Chem.* **49**(6),617-24(2023) Effects of different quenching rate on the various properties of Fe–Si–B amorphous alloy prepared by melt spinning method.
23B061	K.Bolis, G.S.Goulart, A.C.Krohling, R.Mendonca, L.E.Fernandez-Outon*, and J.D.Ardisson*, *ACS OMEGA* **8**(13),12246-58(2023) Structural and magnetic characterization of Nd–Pr–Fe–B sintered magnet machining wastes.
23B063	I.M.Budzulyak, L.S.Yablon, M.M.Khemii, V.O.Kotsyubynsky, B.I.Rachiy, V.MBoychuk, and I.I.Budzulyak, *Fiz. Khim. Tverd. Tila* **24**(4),662-9(2023) Energy state of the electronic subsystem of porous carbon material caused by laser irradiation.
23C033	Y.L.Cao, Y.Xu, S.Khmelevskyi, M.Avdeev, C.W.Wang, S.X.Hu, K.Ohara, Y.H.Xia, X.Chen, Q.Li, J.X.Deng, J.Miao, K.Lin, and X.R.Xing*, *Chem. Mater.* **35**(21),9167-74(2023) Interplanar magnetic orders and symmetry-tuned zero thermal expansion in kagome metal $(Zr,Ta)Fe_2$.
23C034	S.Chakraborty, S.Gupta, V.Bhasin, S.Pakhira, C.Barreteau, J.C.Crivello, S.N.Jha, D.Bhattacharyya, M.Avdeev, V.Paul-Boncour, J.M.Grenèche, E.Alleno, and C.Mazumdar*, *Phys. Rev. B* **108**(24),245151/1-13(2023) Observation of charge transfer induced large enhancement of magnetic moment in a structurally disordered inverse Heusler alloy Fe_2RuGe.
23D033	C.Duchemin, A.I.Liu, J.H.Kim, and P.J.Chirik*, *Organometallics* **42**(21),3109-19(2023) Quinoline pyridine(Imine) iron complexes as catalysts for the 1,4-Hydrovinylation of 1,3-Dienes.
23D034	A.P.Demirov, I.V.Blinkov, D.S.Belov, N.S.Kozlova, E.V.Zabelina, V.M.Kasimova, and V.G.Kostishin, *Inorg. Mater.* **59**(3),272-83(2023) Photocatalytic properties of porous films based on α-Fe_2O_3 hollow microspheres.
23D035	N.Deb, R.Rashid, H.Das, I.M.Syed, and S.M.Hoque*, *R. Soc. Open Sci.* **10**(10),230384(2023) Enhanced specific loss power of hematite-chitosan nanohybrid synthesized by hydrothermal method.
23D036	N.Danyliuk, I.Lapchuk, V.Kotsyubynsky*, V.MBoychuk, and V.Husak*, *Fiz. Khim. Tverd. Tila* **24**(4), 748-60(2023) Effect of Mn^{2+} substitution on catalytic properties of $Fe_{3-x}Mn_xO_4$ nanoparticles synthesized via co-precipitation method.
23E012	O.G.Ellert, E. F.Popova, D.I.Kirdyankin, V.K.Imshennik, E.S.Kulikova, and A.V.Egorysheva*, *Russ. J. Inorg. Chem.* **68**(10),1325-33(2023) Structure and unusual magnetic properties of Mg-containing solid solutions based on Y_2FeTaO_7.
23F016	Y.Fang, K.D.Zhuang, H.Z.Cui, Z.H.Zhang, A.X.Wang, C.M.Wang, D.P.Zheng*, and X.F.Wang, *J. Mater. Chem. A* **11**(47),26193-211(2023) The state of Fe^{3+} in the C-F-A-S-H system with varying Fe/Si and Ca/Si ratios.
23F017	F.Fernandez, M.Otero, M.B.Oviedo, D.E.Barraco, S.A.Paz*, and E.P.M.Leiva, *Phys. Rev. B* **108**(14), 144201/ 1-6(2023) NMR, x-ray, and Mössbauer results for amorphous Li-Si alloys using density functional tight-binding method.
23G044	P.Guzman, C.M.Quine, S.H.Lohaus, L.Schul, R.Toda, V.J.Scott, and B.Fultz, *Rev. Sci. Instrum.* **94**(11), 115107(2023) A miniaturized piezoelectric Mössbauer spectrometer with feedback control.
23G045	I.S.Glazkova, M.N.Smirnova, O.N.Kondrat'eva, G.E.Nikiforova, E.S.Romanova, A.V.Sobolev, I.A.Presniakov, and V.A.Ketsko*, *Russ. J. Inorg. Chem.* **68**(5),547-54(2023) Synthesis and ^{57}Fe Mössbauer studies of polycrystalline magnesium ferrites $MgFe_2O_4$ and $Mg(Fe_{0.8}Ga_{0.2})_2O_4$.
23G046	Y.D.Gritsenko, S.K.Dedushenko*, and Y.D.Perfiliev, *Hyperfine Interact.* **244**(1),26(2023) Mössbauer study of destinezite from Hloubetiń (Czech Republic).
23G047	A.G.Gavriliuk, I.A.Troyan, V.V.Struzhkin, D.N.Trunov, S.N.Aksenov, A.A.Mironovich, A.G.Ivanova, and I.S.Lyubutin, *JETP Lett.* **118**(10),742-53(2023) Synthesis and superconducting properties of some phases of iron polyhydrides at high pressures.
23H035	J.Hadi, J.M.Grenèche, P.Wersin, P.Koho, and B.Pastina, *Clays Clay Miner.* **71**(5),577-99(2023) Determination of sulfide consumption by Fe-bearing components of bentonites.
23H036	M.H.Hoock, O.Leupold, A.Haag, A.Omlor, R.Steinbrugge, I.Sergueev, R.Röhlsberger, H.J.Krüger, J.A.Wolny, and V.Schünemann*, *Hyperfine Interact.* **244**(1),24/1-12(2023) Ir-193 nuclear forward scattering of an iridium(I) complex.
23H038	S.Y.Hu, C.H.Tao*, S.L.Liao, Y.Guan, X.B.Yin, C.W.Zhu, J.Liang, and Z.K.Guo, *Environ. Sci. Technol.* **57**(50), 21438-47(2023) Oxidative dissolution of sulfide minerals tends to accumulate more dissolved heavy metals in deep seawater environments than in shallow seawater environments.

Code	Reference
23K055	I.Koemets, B.Wang, E.Koemets, T.Ishii, Z.D.Liu, C.A.McCammon, A.Chanyshev, T.Katsura, M.Hanfland, A.I.Chumakov, and L.Dubrovinsky*, *Front. Chem. (Lausanne, Switz.)* **11**,1258389/1-10(2023) Crystal chemistry and compressibility of $Fe_{0.5}Mg_{0.5}Al_{0.5}Si_{0.5}O_3$ and $FeMg_{0.5}Si_{0.5}O_3$ silicate perovskites at pressures up to 95 GPa.
23K056	A.S.Kamzin, G.Caliskan, N.Dogan, A.Bingolbali, V.G.Semenov, and I.VBuryanenko, *Tech. Phys.* **68**(12), 602-15(2023) $Zn_xFe_{3-x}O_4$ ($0 \leq x \leq 1.0$) magnetic nanoparticles functionalized with polyacrylic acid (PAA).
23K057	A.A.Krasikov, Y.V.Knyazev, D.A.Balaev*, S.V.Stolyar, V.P.Ladygina, A.D.Balaev, and R.S.Iskhakov, *J. Exp. Theor. Physics* **137**(6),903-13(2023) Magnetic interparticle interactions and superparamagnetic blocking of powder systems of biogenic ferrihydrite nanoparticles.
23K058	Y.Kinoshita, H.Kobayashi, N.Nagasawa, Y.Yoda, R.Masuda, Y.Nakamura, Y.Sakakibara, and K.Deguchi, *Sae Mulli* **73**(12),1145-8(2023) Synchrotron-radiation-based ^{174}Yb Mössbauer spectroscopy of the 1/1 Au-Al-Yb approximant.
23K059	T.Y.Kiseleva, E.V.Lazareva, E.Uyanga, B.Enkhmend, A.S.Komlev, P.Y.Tyapkin, M.V.Il'in, I.P.Ivanenko, G.P.Markov, N.Jargalan, T.F.Grigoreva, and D.Sangaa, *Inorg. Mater.* **59**(11),1220-9(2023) Effect of aluminum substitution on the structural, magnetic, and magnetothermal properties of yttrium iron garnet.
23K060	Z.R.Kadyrova, I.K.Shokosimov, and M.N.Kazakova, *Refract. Ind. Ceram.* **64**(3),240-3(2023) Establishment of the iron-containing phase of gavasay porphyrite by Mössbauer spectroscopy for obtaining basalt fibers.
23K061	T.G.Khonina, D.S.Tishin, A.M.Demin, A.Y.Germov, E.A.Bogdanova, M.S.Karabanalov, and M.S.Valova, *Russ. Chem. Bull.* **72**(12),2791-8(2023) Nanocomposite material based on Fe_3O_4 magnetic nanoparticles modified with iron and silicon glycerolates: synthesis and characterization.
23K062	S.N.Kane, R.Verma, S.S.Modak, V.R.Reddy, and F.Mazaleyrat, *Hyperfine Interact.* **244**(1),3(2023) Structural, Mössbauer and magnetic study of $Co_{1-x}Zn_xFe_2O_4$ (x=0.0 - 0.56) nano ferrites.
23L055	Z.W.Li, Y.Xie, J.X.Gao, X.K.Zhang, J.Zhang, Y.Liu, and G.Li*, *J. Mater. Chem. A* **11**(48),26573-9(2023) The promotional effect of multiple active sites on Fe-based oxygen reduction electrocatalysts for a zinc-air battery.
23L056	T.J.Li, X.C.Huang*, Z.R.Ma, B.Li, X.Y.Wang, and L.F.Zhu*, *Phys. Rev. A* **108**(3),033715/1-9(2023) Fano-Lorentz shape controlled by the collective effect of the nuclear ensemble.
23L057	K.P.Lindquist, A.Eghdami, C.R.Deschene, A.J.Heyer, J.J.Wen, A.G.Smith, E.I.Solomon, Y.S.Lee, J.B.Neaton, D.H.Ryan, and H.I.Karunadasa*, *Nature Chem.* **15**(12),1780-6(2023) Stabilizing Au^{2+} in a mixed-valence 3D halide perovskite.
23M054	D.H.Moon, N.R.Lee, W.R.Han, S.J.Kim, and Y.R.Uhm*, *J. Radioanal. Nucl. Chem.* **332**(12),5175-84(2023) Characterization of iron oxides-based red pigments in the ancient Gaya region, South Korea.
23M055	J.Mosrati, T.Ishida, H.Mac, M.Al-Yusufi, T.Honma, M.Parliniska-Wojtan, Y.Kobayashi, A.Klyushin, T.Murayama*, and A.M.Abdel-Mageed*, *Angew. Chem., Int. Ed.* **62**(51),e202311340(2023) Low-temperature hydrogenation of CO_2 to methanol in water on ZnO-supported CuAu nanoalloys.
23M056	K.Młynarek-Zak, I.Dhiman, K.Matus, M.Kadziolka-Gawel, W.Loński, A.Radon, T.Czeppe, and R.Babilas*, *Sci. Rep.* **13**(1),21322(2023) Structural characterization of newly-developed $Al_{79}Ni_5Fe_5Y_{11}$ and $Al_{79}Ni_{11}Fe_5Y_5$ alloys with amorphous matrixes.
23M057	M.E.Matsnev, and V.S.Rusakov*, *Phys. Met. Metallogr.* **124**(10),1068(2023) Erratum to: the creation of complex multi-component models of Mössbauer spectra based on the example of a study of hyperfine interactions in quasi-binary alloys with the laves phase structure.
23M058	A.V.Marchenko, E.I.Terukov, F.S.Nasredinov, Y.A.Petrushin, and P.P.Seregin*, *Tech. Phys.* **68**(S1),S88-95(2023) Local structure of amorphous $(GeTe)_x(Sb_2Te_3)$ films.
23N028	D.Nam, J.P.Bacik, R.L.Khade, M.C.Aguilera, Y.Wei, J.D.Villada, M.L.Neidig*, Y.Zhang*, N.Ando*, and R.Fasan*, *Nat. Commun.* **14**(1),7985(2023) Mechanistic manifold in a hemoprotein-catalyzed cyclopropanation reaction with diazoketone.
23P036	A.Pedersen, A.Bagger, J.Barrio, F.Maillard, I.E.L.Stephens, and M.M.Titirici*, *J. Mater. Chem. A* **11**(43), 23211-22(2023) Atomic metal coordinated to nitrogen-doped carbon electrocatalysts for proton exchange membrane fuel cells: a perspective on progress, pitfalls and prospectives.
23P037	D.Popov, R.G.Batulin, M.A.Cherosov, F.G.Vagizov, A.L.Zinnatullin, T.Chupakhina, Y.Deeva, T.Maiti, and R.Eremina*, *Magnetochemistry* **9**(10),219/1-14(2023) Phase separation in the double perovskite $Sr_2FeNbO_{6-\delta}$.
23P038	J.C.Paris, S.Hu, A.W.Wen, A. C.Weitz, R.H.Cheng, L.B.Gee, Y.J.Tang, H.Kim, A.Vegas, W.C.Chang*, S.J.Elliott*, P.H.Liu*, and Y.S.Guo*, *Angew. Chem., Int. Ed.* **62**(43),e202309362/1-8(2023) An S=1 iron(IV) intermediate revealed in a non-heme iron enzyme-catalyzed oxidative C-S bond formation.
23P039	A.Pisarikova, J.Olejnicek, I.Venkrbcova, L.Nozka, S.Cichon, A.Azinfar, R.Hippler, C.A.Helm, M.Maslan, L.Machala, and Z.Hubicka, *J. Vac. Sci. Technol., A* **41**(6),063005/1-14(2023) $CuFeO_2$ prepared by electron

Code	Reference
	cyclotron wave resonance-assisted reactive HiPIMS with two magnetrons and radio frequency magnetron sputtering.
23P040	V.S.Pokatilov, V.S.Rusakov, A.M.Gapochka*, and A.S.Sigov, *Crystallogr. Rep.* **68**(5),779-87(2023) Spatial spin-modulated structure of $Bi_{1-x}Sr_xFeO_{3-y}$ (x=0, 0.05, and 0.10) multiferroics.
23P041	I.Popov, D.Raenko, A.Tchougreeff*, and E.Besley*, *J. Phys. Chem. C* **127**(44),21749-57(2023) Electronic structure and d-d spectrum of metal-organic frameworks with transition-metal ions.
23P042	K.Pandey, R.C.Srivastava, R.Dhyani*, P.S.Rawat, and G.Dixit, *J. Supercond. Novel Magn.* **36**(10-12), 1901-11(2023) Impact of rare earth ions (Ce and Gd) on structural and magnetic properties of nanostructured Ni-Zn ferrites.
23P043	L.V.Panova, D.A.Lemenovskii, M.I.Afanasov, D.P.Krut'ko, M.A.Popkov, R.O.Burlutskiy, M.M.Brusova, M.Koel, Y.Bolobajev, V.N.Talanova, and A.G.Buyanovskaya, *Russ. J. Phys. Chem. B* **17**(7),1526-33(2023) Ferrocene-modified resorcinol-formaldehyde aerogels.
23R027	C.K.Ribeiro, A.F.Rabello, V.Martelli, I.Zivkovic, E.Fogh, H.M.Ronnow, D.R.Cornejo, and J.L.Jimenez*, *New Phys.: Sae Mulli* **73**(12),1149-54(2023) Electrical and magnetic properties of $FeGa_3$ with antisite disorder.
23S070	V.Stagno, L.Bindi, B.Bonechi, S.Greaux, A.Aulbach, T.Irifune, S.Lupi, G.Marras, C.A.McCammon, M.Nazzari, F.Piccirilli, B.T.Poe, C.Romano, and P.Scarlato, *Sci. Rep.* **13**(1),15855(2023) Cubic Fe-bearing majorite synthesized at 18-25 GPa and 1000 °C: implications for element transport, subducted slab rheology and diamond formation.
23S085	P.Saha, S.Barman, SAmanullah, and A.Dey*, *ACS Catal.* **13**(20),13181-94(2023) Selective electrocatalytic reduction of NO to NH_3 by iron porphyrins at physiologically relevant potentials.
23S086	K.Scanda, Y.Avila, L.Sanchez, R.Mojica, B.Portales-Martinez, M.Gonzalez, M.Avila*, and E.Reguera*, *J. Phys. Chem. C* **127**(44),21777-87(2023) Adsorption of aromatic molecules in a microporous spin crossover material, Fe(pyrazine)[$Fe(CN)_5NO$]. Tuning of its physical properties.
23S087	K.Scanda, Y.Avila, L.Sanchez, R.Mojica, M.Gonzalez, B.D.Moreno*, M.Avila*, and E.Reguera*, *New J. Chem.* **47**(47),21834-44(2023) Thermally-induced spin-crossover (SCO) in Fe(4-ethynylpyrdine)$_2$[$Fe(CN)_5NO$]. Why is the SCO observed in 2D ferrous nitroprussides despite the NO-NC repulsive interaction in the interlayer region?.
23S088	D.Singh, Y.Hu, S.S.Meena, R.Vengarathody, M.Fichtner, and P.Barpanda*, *Chem. Commun. (Cambridge, U. K.)* **59**(97),14391-4(2023) Iron-based fluorophosphate Na_2FePO_4F as a cathode for aqueous zinc-ion batteries.
23S089	E.A.Stroganova, S.M.Kazakov, P.B.Fabrichnii, M.I.Afanasov, and A.N.Kuznetsov*, *Russ. J. Inorg. Chem.* **68**(12), 1714-24(2023) Vanishing superstructure: crystal and local structures of $Ni_{3-x}MTe_2$ (M=Sb, Sn).
23S090	M.N.Shipko, V.V.Korovushkin, M.A.Stepovich, and A.V.Trukhanov, *Bull. Russ. Acad. Sci.: Phys.* **87**(11), 1729-31(2023) Modifying the local structure and properties of zinc-substituted hexagonal barium ferrites for microwave devices via magnetic pulse processing.
23S091	S.V.Stolyar, O.A.Li, E.D.Nikolaeva, A.M.Vorotynov, D.A.Velikanov, Y.V.Knyazev, O.A.Bayukov, R.S.Iskhakov, O.V.Kryukova, V.F.Pyankov, M.N.Volochaev, and A.A.Mokhov, *Phys. Met. Metallogr.* **124**(14),1689-96(2023) Preparation and properties of magnetic composites γ-Fe_2O_3/SiO_2/aptamer(FAS9) for magnetic resonance hyperthermia.
23S092	K.Schulz, L.Notini, A.R.C.Grigg, L.Joëlle Kubeneck, W.Wisawapipat, L.K.ThomasArrigo*, and R.Kretzschmar, *Environ. Sci.: Processes Impacts* **25**(12),1945-61(2023) Contact with soil impacts ferrihydrite and lepidocrocite transformations during redox cycling in a paddy soil.
23S093	S.A.Semenov, R.V.Saprykin, G.I.Dzhardimalieva, K.V.Pokholok, M.C.Balashov, A.I.Ivanova, and V.I.Popenko, *Nanobiotechnol. Rep.* **18**(S2),S256-67(2023) Synthesis and properties of nanocomposites based on iron(III) salts of saturated monocarboxylic acids.
23S095	N.A.Sanina, A.N.Utenyshev, P.V.Dorovatovskii, N.S.Emel'yanova, N.S.Ovanesyan, A.V.Kulikov, I.V.Sulimenkov, V.B.Luzhkov, O.V.Pokidova, and S.M.Aldoshin, *Dalton Trans.* **52**(47),18090-101(2023) Synthesis of a tetranitrosyl iron complex with unique structure and properties as an inhibitor of phosphodiesterases.
23S096	M.Sakurai, T.Ueta, and C.Joachim, *J. Environment Sci.* **9**(10),2300347/1-8(2023) Weakly interacting molecular spins in on-surface synthesized nanoclusters on a graphene oxide nanosheet.
23T019	E.K.Tripoliti, D.P.Dobson, A.D.Fortes, A.R.Thomson, P.F.Schofield, and I.G.Wood*, *Mineral. Mag.* **87**(6), 789–806(2023) Structure and thermal expansion of end-member olivines I: crystal and magnetic structure, thermal expansion, and spontaneous magnetostriction of synthetic fayalite, Fe_2SiO_4, determined by high-resolution neutron powder diffraction.
23T021	Y.A.Teterin, M.N.Smirnova, K.I.Maslakov, A.Y.Teterin, G.E.Nikiforova, Y.S.Glazkova, A.N.Sobolev,

Code	Reference
	I.A.Presnyakov, and V.A.Ketsko*, *Russ. J. Inorg. Chem.* **68**(7),829-37(2023) Synthesis, ionic, and phase compositions of ferrogarnet $Y_{2.5}Ce_{0.5}Fe_{2.5}Ga_{2.5}O_{12}$.
23U006	A.I.Ulyanov, A.A.Chulkina, A.L.Ulyanov*, and V.E.Porsev, *Khim. Fiz. Mezoskopiya* **25**(1),46-56(2023) Application of Mössbauer spectroscopy to comprehensive investigation of phase composition, phase magnetic state of mechanically synthesized Fe-Mn-Ni-C Nanocomposites. (In Russian)
23U007	P.G.Undre, A.V.Humbe*, J.S.Kounsalye, A.Kumar, R.V.Kathare, and K.M.Jadhav, *J Inorg Organomet Polym* **33**(11),3372-88(2023) Diamagnetic Al^{3+} doped Ni-Zn spinel ferrite: rietveld refinement, elastic, magnetic, Mössbauer, and electrical explorations.
23W026	L.Wolff, and J.Evers*, *Phys. Rev. A* **108**(4),043714/1-20(2023) Characterization and detection method for x-ray excitation of Mössbauer nuclei beyond the low-excitation regime.
23W027	L.X.Wang, L.J.Rao, M.X.Ran, Q.K.Shentu, Z.L.Wu, W.K.Song, Z.W.Zhang, H.Li, Y.Y.Yao, W.Y.Lv*, and M.Y.Xing*, *Nat. Commun.* **14**(1),7841(2023) A polymer tethering strategy to achieve high metal loading on catalysts for Fenton reactions.
23W028	M.Wysocka-Zolopa, K.Wojtulewski, A.Basa, D.Satula, K.H.Markiewicz, E.Gradzka, and K.Winkler*, *Macromol. Rapid Commun.* **44**(22),2300387/1-15(2023) Investigation of magnetic electrodes in conducting polymeric materials: electrochemical properties of a fullerene[C60]-Pd polymer and iron oxide magnetic nanocomposite.
23Y020	Y.C.Yao, T.Jiang, S.Y.Lim, C.Frandsen, Z.J.Li, Y.B.Dou, F.Y.Wu, J.B.Qin, J.Z.Zou, E.Stamate, and W.J.Zhang*, *Small* **19**(49),2304655/1-10(2023) Universal synthesis of half-metallic diatomic catalysts for efficient oxygen reduction electrocatalysis.
23Y021	F.F.Yan, D.Liu, R.Cai, L.Zhao, P.D.Mao, H.Y.Sun, Y.S.Meng*, and T.Liu*, *Dalton Trans.* **52**(48),18206-13(2023) Simultaneous magneto-dielectric transitions in a fluorescent Hofmann-type coordination polymer.
23Y022	J.Yoon, J.Lee, S.J.Ye, and Y.B.Bang*, *Sci. Rep.* **13**(1),19856(2023) Development of an advanced velocity modulator for a portable Mössbauer spectrometer.
23Y023	V.A.Yerokhin, and N.S.Oreshkina*, *Phys. Rev. A* **108**(5),052824/1-6(2023) QED calculations of the nuclear recoil effect in muonic atoms.
23Z042	B.Zhang, W.Ren, S.Y.Yang, Q.F.Kuang, D.Li, X.Liu, A.M..Zhang, H.Pang, L.Y.Tang, L.Qiao, F.S.Li, and Z.W.Li*, *Phys. Rev. B* **108**(21),214401/1-9(2023) Mössbauer spectroscopy study of magnetostructural and spin-state transitions in the breathing pyrochlore $LiFeCr_4O_8$.
23Z043	C.Zeng, Q.D.Xu, X.L.Liu, S.M.Hu, X.T.Wu, and T.L.Sheng*, *Dalton Trans.* **52**(45),16858-69(2023) Different delocalized ranges in mixed valence cyanido-metal-bridged Fe-Ru-Fe complexes controlled by terminal ligand substitution modification.
24A004	K.As, S.Peiffer, P.O.Uhuegbue, P.A.Joshi, A.Kappler, B.Marouane, and K.Hockmann, *Chem. Geol.* **653**, 122043(2024) Sulfate affinity controls phosphate sorption and the proto-transformation of schwertmannite.
24B002	A.Banerjee, A.Das, A.Roychowdhury, A.Saha, D.Das, and S.Sarkar, *J. Magn. Magn. Mater.* **595**,171927(2024) A systematic study of oxygen vacancy mediated short range and long range magnetic ordering in $BaTi_{1-x}Fe_xO_3$ (x=0.02).
24B003	J.Brehme, M.S.Kilic, J.Pawlak, F.Renz, and R.F.Sindelar, *Interactions (Cham, Switz.)* **245**(1),10/1-13(2024) Soluble molecular switches in electrospun nanofibers.
24B004	C.Belloni, L.Korving, G.J.Witkamp, E.Bruck, and A.I.Dugulan, *Colloids Surf., A* **687**,133476(2024) Zn induced surface modification of stable goethite nanoparticles for improved regenerative phosphate adsorption.
24B005	M.Baricic, P.Maltoni*, G.Barucca, N.Yaacoub, A.Omelyanchik, F.Canepa, R.Mathieu, and D.Peddis*, *Phys. Chem. Chem. Phys.* **26**(7),6325-34(2024) Chemical engineering of cationic distribution in spinel ferrite nanoparticles: the effect on the magnetic properties.
24B006	V.Bilovol, R.Martinez Garcia, M.Pagnola, S.Ferrari, F.Morales, J.Zukrowski, and M.Sikora, *J. Magn. Magn. Mater.* **596**,171913(2024) Al-doped $BaFe_{12}O_{19}$ hexaferrites: dopant distribution in the crystal lattice and its effect on the magnetic order.
24B007	A.Baral, C.Pesce, A.S.Yorkshire, Z.Zhakiyeva, R.Snellings, T.Hanein*, J.L.Provis, and A.Peys*, *Cem. Concr. Res.* **177**,107419(2024) Characterisation of iron-rich cementitious materials.
24B008	K.Bharuth-Ram, C.Ronning, and H.Hofsass, *Interactions (Cham, Switz.)* **245**(1),12/1-7(2024) Formation of magnetic nanoclusters in Fe implanted amorphous and crystalline SiO_2.
24B009	V.Bilovol, J.Zukrowski, M.Sikora, P.Novak, K.Berent, and D.Rybicki, *J. Mol. Struct.* **1305**,137780(2024) Low-temperature Mössbauer spectroscopy: evaluation of cation distribution in $CoFe_2O_4$.
24C003	X.Z.Chang, and Q.L.Chen*, *Mater. Chem. Phys.* **317**,129154(2024) Magnetically engineering enhanced EMA property through high entropy transition metal ions within all-inorganic perovskite.

Code	Reference
24D002	S.T.Dlamini, T.Moyo, A.Nhlapo*, D.Wamwangi, A.Akande, and B.W.Mwakikunga, *J. Mol. Struct.* **1305**, 137789(2024) Study of microstructure, magnetic and gas sensing properties of porous $N_{0.4+x}Zn_{0.6-x}Ce_yFe_{2-y}O_4$ magnetic nanoparticles.
24D003	B.Dey, C.Manoharan*, M.Venkateshwarlu, C.S.Pawar, and S.Sagadevan, *Ceram. Int.* **50**(7_Part_B), 12121-35(2024) Exploring the effect of zinc substitution in nanocrystalline nickel ferrite for enhanced supercapacitor and gas sensing applications.
24D004	E.M.Davis, E.L.Ribeiro, S.Kamali, J.G.Wen, C.E.Johnson, J.A.Johnson*, B.Khomami, and D.Mukherjee*, *Appl. Surf. Sci.* **658**,159682(2024) Fe-carbide/Fe-oxide-based nanocomposites synthesized as magnetic nanomaterials via laser ablation synthesis in solution (LASiS).
24Q001	Y.Q.Qian, L.Xiao*, J.W.Zhao, J.W.Head, Q.He, H.R.Xu, F.Z.Wang, X.P.Zhang, X.Q.Ping, W.Zeng, X.Wang, J.Michalski, J.C.Liu, B.L.Ye, M.Z.Wang, L.Z.Sun, Y.Pang, J.Wang, and S.Y.Zhao, *Icarus* **410**,115892(2024) First magnetic and spectroscopic constraints on attenuated space weathering at the Chang'e-5 landing site.
24W002	Y.H.Wang, P.Fu, H.Takatsu, C.Tassel, N.Hayashi, J.J.Cao, T.Bataille, H.J.Koo, Z.W.Ouyang, M.H.Whangbo, H.Kageyama*, and H.C.Lu*, *J. Am. Chem. Soc.* **146**(12),8320-6(2024) Construction of ideal one-dimensional spin chains by topochemical dehydration/rehydration route.

Source	Absorber	Temp	IS	QS	Comments	Code
Au-197 77.40 keV Transition						
^{197}Pt in Pt foil prepared through neutron irradiation	Au foil and catalysts having Cu+Au loadings of: 1 wt % $Cu_{93}Au_7$/ZnO, 3 wt % $Cu_{93}Au_7$/ZnO; and 5 wt % $Cu_{93}Au_7$/ZnO	300	--	--	calculated the Au percentages (from IS increasing linearly with Au content) to be 2.7, 9.2, and 9.4 mol% for $Cu_{93}Au_7$/ZnO of 1, 3 and 5 wt%, respectively	23M055
^{197}Pt created by neutron activation of a 100 mg piece of enriched ^{196}Pt	mixed-valence perovskite $Cs_4Au^{II}Au^{III}_2Cl_{12}$	10	--	--	identified the doublets assigned to Au^{3+} (67%) and Au^{2+}(33%)	23L057
Fe-57 14.40 keV Transition: Biological Compounds						
Rh(IS/α-Fe)	biogenic ferrihydrite manoparticles before and after low-temperature annealing at 150°C in air for 24 h	v	--	--	sites of Fe1, Fe2 and Fe3 are identified with 3 doublets at 300 K and with three sextets at 4.2 K	23K057
Rh(IS/α-Fe)	complex OvoA•Fe(II)•Cys•His	4.2	1.17	3.12	a typical high-spin (S=2) ferrous species found in non-heme iron-containing enzymes identical to the OvoA quaternary complex	23P038
Rh(IS/α-Fe)	complexes {FeDEsP-NO}$_7$ and {FeTEsP-NO}$_7$ before adding cobaltocene, and after adding cobaltocene	90	--	--	the addition of cobaltocene resulted in the appearance of additional doublets assigned to {FeDEsP-NO}$_8$ and {FeTEsP-NO}$_8$	23S085
Rh(IS/α-Fe)	ferrous protein, after incubation with $Na_2S_2O_4$, and Mb-cIII, trapped after further incubation	300	--	--	identified the low-spin iron (II) species with an isomer shift (δ) of 0.47mm/s and a quadrupole splitting ($\|\Delta E_Q\|$) of 1.00 mm/s before and HS Fe(II) after carbene moiety is transferred to a ring nitrogen atom of the porphyrin cofactor (δ=0.97mm/s and $\|\Delta E_Q\|$=4.00mm)	23N028
Rh(IS/α-Fe)	frozen solutions of reaction at various time points of OvoA•Fe(II)•Cys•His with O_2 without and with the presence of Cld and ClO_2: anaerobic OvoAMtht · Fe(II) ·Cys· His quaternary complex, Int490 reactive intermediate, and enzyme-product complex	4.2	--	--	Int490 exhibited a large axial zero field splitting (D=30 cm^{-1}), and an axial ^{57}Fe nuclear hyperfine tensor (Ax/gnβ*n*=Ay/gnβ*n*=-26 T, Az/gnβ*n*=-5 T), best comparable with the heme-based S=1 oxoferryl intermediates from Mb	23P038
Rh(IS/α-Fe)	Nanoparticles of $MnFe_2O_4$,Fe_3O_4, and $CoFeO_4$ coated with PLLA-PVA capsules	v	--	--	identified sextets of A and B sites for $MnFe_2O_4$, and $CoFeO_4$, and A, B2, B2 sites for Fe_3O_4	23A040
Rh(IS/α-Fe)	of iron oxide (α-Fe_2O_3) nanoparticles functionalized with chitosan synthesized by hydrothermal method	300	--	--	observed spectra modelled with a doublet and 3 sextets or a sextet with the asymmetric line broadening assigned to a mixed slow-fast relaxation	23D035
Rh(IS/α-Fe)	$Zn_xFe_{3-x}O_4$ (for *x*=0, 0.25, 0.5, 0.75 and 1.0) functionalized with polyacrylic acid $Zn_xFe_{3-x}O_4$@PAA	300	--	--	modelled the spectra with the sextet subspectra of A, B1, B2, B3 and B4 for *x*=0; A, B1, B2 and a surface-like collapsed sextet for *x* = 0.25; A, B1, surface-collapsed S, and doublet D for *x*=0.5; A+B, surface-collapsed S, and doublet D for *x*=0.75; and doublets D1,D2 and impurity(Fe_2O_3) sextet for *x*=1	23K056
Fe-57 14.40 keV Transition: Catalysts						
Rh(IS/α-Fe)	(L2)$FeCH_3$ quinoline pyridine(imine) iron complex (QPI = N-(2,6-dimethylphenyl)-1-(6-(quinolin-2-yl)-pyridin-2-yl)ethan-1-imine)	80	0.53	1.27	identified the antiferromagnetic coupling of HS Fe(II) to a singly reduced (QPI1−) ligand with a total spin of (S=3/2)	23D033
Rh(IS/α-Fe)	Catalyst Fe@N-C-800	300	--	--	modelled the spectra with the 4 sextets identified with α-Fe (64%), Fe_3O_4 and iron carbide, and a doublet D1 (12%)	23W027
Rh(IS/α-Fe)	complex OvoA•Fe(II)•Cys•His	4.2	1.17	3.12	a typical high-spin (S=2) ferrous species found in non-heme iron-containing enzymes identical to the OvoA quaternary complex	23P038
Rh(IS/α-Fe)	complexes {FeDEsP-NO}$_7$ and {FeTEsP-NO}$_7$ before adding cobaltocene, and after adding cobaltocene	90	--	--	the addition of cobaltocene resulted in the appearance of additional doublets assigned to {FeDEsP-NO}$_8$ and {FeTEsP-NO}$_8$	23S085
Rh(IS/α-Fe)	diatomic catalyst Fe, Zn-N-C	v	--	--	diatomic catalyst has a larger proportion of the D2 site assigned to ferrous iron with a medium spin state	23Y020
xx	Fe-N-C catalysts	v	--	--	reviewed the ex-situ, in situ, and operando Mössbauer spectroscopy in Fe-N-C	23P036
Cr(IS/α-Fe)	$Fe_{3-x}Mn_xO_4$ 0.00<*x*<0.25 nanoparticles synthesized via co-precipitation method	300	--	--	observed no spm-relaxation and suggested that the ferrite particle size is above 4.2-4.6 nm	23D036

Source	Absorber	Temp	IS	QS	Comments	Code
Rh(IS/α-Fe)	ferrous protein, after incubation with $Na_2S_2O_4$, and Mb-cIII, trapped after further incubation	300	--	--	identified the low-spin iron (II) species with an isomer shift (δ) of 0.47mm/s and a quadrupole splitting ($\|\Delta E_Q\|$) of 1.00 mm/s before and HS Fe(II) after carbene moiety is transferred to a ring nitrogen atom of the porphyrin cofactor (δ=0.97mm/s and $\|\Delta E_Q\|$=4.00mm)	23N028
Rh(IS/α-Fe)	frozen solutions of reaction at various time points of OvoA•Fe(II)•Cys•His with O_2 without and with the presence of Cld and ClO_2: anaerobic OvoAMtht · Fe(II) ·Cys· His quaternary complex, Int490 reactive intermediate, and enzyme-product complex	4.2	--	--	Int490 exhibited a large axial zero field splitting (D=30 cm^{-1}), and an axial ^{57}Fe nuclear hyperfine tensor (Ax/gnβ*n*=Ay/gnβ*n*=-26 T, Az/gnβ*n*=-5 T), best comparable with the heme-based S=1 oxoferryl intermediates from Mb	23P038
Rh(IS/α-Fe)	Hm/C_y@C-900 and Hm/TCA@C-900 electrocatalysts	300	--	--	identified the actual iron components to be the phases of Fe_3C, FeS_x, Fe_3O_4, and metallic alpha-Fe nanoparticles	23L055
Rh(IS/α-Fe)	hollow α-Fe_2O_3 microspheres produced by spray pyrolysis	v	--	--	identified major (86%) and minor (14%) sextets assigned to bulk (B_{hf}=51.4 T) and surface (B_{hf}=49 T)	23D034
Rh(IS/α-Fe)	neutral tetranitrosyl iron complex $\{[Fe(H_2O)_4]^{2+}[FeR_2(NO)_2]_2^{2-}\}\cdot 4H_2O$ with R=5-(3-pyridyl)-4H-1,2,4-triazole-3-thiolyls	295	--	--	identified two doublets with intensity ratio of 2:1, assigned to Fe(I)LS (major) and Fe(II)LS (minor)	23S095
Fe-57 14.40 keV Transition: FERROMAGNETIC						
Rh(IS/α-Fe)	$BaFe_{11.75}Zn_{0.25}O_{19}$ ferrite before and after magnetic pulse processing	300	--	--	both averaged B_{hf} and QS decrease with increasing the time of magnetic pulse processing	23S090
Rh(IS/α-Fe)	$BaFe_{12-x}Al_xO_{19}$ (*x*=0, 0.5, 1.0, 1.5)	300	--	--	identified 5 sextets assigned to the sites: three octahedral (2a, $4f_2$, and 12 k), one tetrahedral ($4f_1$) and one trigonal bipyramidal (2b)	24B006
Rh(IS/Fe)	$BaTi_{1-x}Fe_xO_3$(*x*=0.02)	300	--	--	identified a doublet and detected a presence of 2 minor impurity sextets attributed to the impurity ordering of both FM and AFM types among Fe^{3+}	24B002
Rh(IS/α-Fe)	CE-5 lunar soil CE5C0600	300	--	--	applied a fitting model of a sextet (alpha-Fe, 2.5%) and three Fe^{2+} doublets: D1 (ilmenite, 9%), D2 (pyroxene M1+olivine, 33%) and D3 (pyroxene M2+glass, 55%)	24Q001
Rh(IS/α-Fe)	$Co_{1-x}Zn_xFe_2O_4$ (*x*=0.0-0.56) ferrites synthesized by sol-gel autocombustion	v	--	--	spectra are a combination of broad sextet, and a dominant paramagnetic doublet with QS of 0.70 – 0.84 mm/s, and the doublet area range between 20 – 50%	23K062
Rh(IS/α-Fe)	Heusler alloy Fe_2RuGe	v	--	--	identified three Fe sites with the relative absorption areas of 55%, 23%, and 22% for the three sites Fe-4b, Fe-4c, and Fe-4d, with <B_{hf}> at 300 K of 30.6, 23.3, and 21.8 T	23C034
Rh(IS/α-Fe)	hollow α-Fe_2O_3 microspheres produced by spray pyrolysis	v	--	--	identified major (86%) and minor (14%) sextets assigned to bulk (B_{hf}=51.4 T) and surface (B_{hf}=49 T)	23D034
Rh(IS/α-Fe)	iron polyhydrides FeH_x synthesized with ^{57}Fe at 178 and 195 GPa	300	--	--	reviewed the previous Mössbauer data showing that the hydride phase is magnetically ordered according to the Mössbauer spectroscopy data	23G047
Rh(IS/α-Fe)	Kagomé Metal (Zr,Ta)Fe^2 annealed at different temperatures (1473K and 1073K)	300	--	--	identified 4 magnetically inequivalent Fe sites (6h, 2a and two 16d) and determined the ratio and hyperfine field of each Fe atoms	23C033
Rh(IS/α-Fe)	$LiFeCr_4O_8$	v	--	--	determined the temperature dependence of hyperfine parameters showing the ferrimagnetic transition at T_N ~ 94 K, the spin-gap transition at T_{SG} ~ 50 K, and the magnetostructural transition at T_{MS} ~ 19 K	23Z042
Rh(IS/α-Fe)	metal-nanocomposites Fe-Mn-Ni-C synthesized by mechanical milling	v	--	--	identified magnetic ferrite, austenite (paramagnetic and ferromagnetic), and cementite (both paramagnetic and ferromagnetic))	23U006
Rh(IS/α-Fe)	$MgFe_2O_4$ and $Mg(Fe_{0.8}Ga_{0.2})_2O_4$ prepared by auto-combustion method	v	--	--	performed measurements at 776 K and at 14 K and obtained the ratios of the intensities of the partial for two iron positions, I(FeA)/I(FeB), ~0.72 and ~0.89 for $MgFe_2O_4$ and $Mg(Fe_{0.8}Ga_{0.2})_2O_4$, respectively	23G045
Rh(IS/α-Fe)	multiferroics $Bi_{1-x}Sr_xFeO_{3-y}$ (*x* =0, 0.05, and 0.10)	300	--	--	identified three P(B_{hf}) distributions, each described within the model of cycloid spatial anharmonic spin modulation	23P040
Rh(IS/α-Fe)	$MxCo_{1-x}Fe_2O_4$ (M^{2+} =Ni^{2+}, Zn^{2+})	v	--	--	identified A and B sites; determined the cation distribution and observed a small Zn^{2+} quantity in Oh-sites.	24B005
Rh(IS/α-Fe)	γ-Fe_2O_3 and γ-Fe_2O_3/SiO_2	300	--	--	coating of nanoparticles leads to a change in the fraction of the superparamagnetic doublet and relaxational component	23S091

Source	Absorber	Temp	IS	QS	Comments	Code
Fe-57 14.40 keV Transition: Frozen Solutions						
Rh(IS/α-Fe)	complex OvoA•Fe(II)•Cys•His	4.2	1.17	3.12	a typical high-spin (S=2) ferrous species found in non-heme iron-containing enzymes identical to the OvoA quaternary complex	23P038
Rh(IS/α-Fe)	complexes {FeDEsP-NO}$_7$ and {FeTEsP-NO}$_7$ before adding cobaltocene, and after adding cobaltocene	90	--	--	the addition of cobaltocene resulted in the appearance of additional doublets assigned to {FeDEsP-NO}$_8$ and {FeTEsP-NO}$_8$	23S085
Rh(IS/α-Fe)	frozen solutions of reaction at various time points of OvoA•Fe(II)•Cys•His with O_2 without and with the presence of Cld and ClO_2: anaerobic OvoAMtht · Fe(II) ·Cys· His quaternary complex, Int490 reactive intermediate, and enzyme-product complex	4.2	--	--	Int490 exhibited a large axial zero field splitting (D=30 cm^{-1}), and an axial ^{57}Fe nuclear hyperfine tensor (Ax/gnβ*n*=Ay/gnβ*n*=-26 T, Az/gnβ*n*=-5 T), best comparable with the heme-based S=1 oxoferryl intermediates from Mb	23P038
Rh(IS/α-Fe)	iron(III)-peroxo complex bearing an N-tetramethylated cyclam ligand, $[Fe^{III}(O_2)(12\text{-TMC})]^+$	4.2	0.53	--	demonstrated paramagnetic relaxation of a single species having an S=5/2 spin state a small axial zero-field splitting (D=−1 cm^{-1}), a large rhombic zero-field splitting (E/D=0.31), and a close-to-is otropic A tensor ([−20.0, −20.0, −21.2] T)	23Y023
Fe-57 14.40 keV Transition: Glasses and Amorphous Substances						
Rh(IS/α-Fe)	$Al_{79}Ni_5Fe_5Y_{11}$ and $Al_{79}Ni_{11}Fe_5Y_5$ alloys	v	--	--	performed a fit with 2 QS distributions and assigned Fe with higher QS to mainly aluminium and yttrium surrounding, and Fe with lower QS to iron atoms surrounded mainly by aluminium and nickel atoms	23M056
Rh(IS/α-Fe)	amorphous SiO_2 implanted with 60 keV ^{57}Fe	300	--	--	identified sextet components (B_{hf}=3.5 T, 31.1T and 29.1 T) consistent with the precipitation of metallic α-Fe nanoclusters, and doublets, assigned to Fe^{2+} and Fe^{3+} species	24B008
Rh(IS/α-Fe)	crystalline SiO_2 implanted with 60 keV ^{57}Fe	300	--	--	identified high-B_{hf} sextet components (B_{hf}=52.7 T and 52.3 T) consistent with the precipitation of α-Fe_2O_3 and a doublet, assigned to Fe^{3+} species	24B008
Rh(IS/α-Fe)	disordered gel with a crosslinked structure of $CaO–Fe_2O_3–Al_2O_3–SiO_2–H_2O$	300	--	--	identified two kinds of octahedral Fe^{3+}: the distorted one (modifier), and more symmetric (a layer former)	23F016
Rh(IS/α-Fe)	hollow α-Fe_2O_3 microspheres produced by spray pyrolysis	v	--	--	identified major (86%) and minor (14%) sextets assigned to bulk (B_{hf}=51.4 T) and surface (B_{hf}=49 T)	23D034
Fe-57 14.40 keV Transition: High Temperature Superconductors						
Rh(IS/α-Fe)	iron polyhydrides FeH_x synthesized with ^{57}Fe at 178 and 195 GPa	300	--	--	reviewed the previous Mössbauer data showing that the hydride phase is magnetically ordered according to the Mössbauer spectroscopy data	23G047
Fe-57 14.40 keV Transition: Inorganic Cyanides						
Rh(IS/α-Fe)	Fe(4-ethynylpyrdine)$_2$[Fe(CN)$_5$ NO]	v	--	--	identified 2 Fe(II) LS subspectra at 5 K and the Fe(II)LS + Fe(II) HS subspectra at 295 K	23S087
Rh(IS/α-Fe)	$Fe(Py_2)$[Fe-(CN)$_5$NO] before and after insertion the guest species (benzene/toluene or furan/thiophene)	5	--	--	identified the Fe(II) LS and HS doublets; the guest-host interaction is favorable to the SCO for benzene and toluene and unfavorable for furan and thiophene	23S086
Rh(IS/α-Fe)	polymer {Fe(DPPE)$_2$[Ag(CN)$_2$]$_2$}·2EtOH with a luminescent ligand DPPE=1,1-diphenyl-2,2-di(4-py ridylbiphenyl)ethylene	40	--	--	identified the doublet subspectra for the LS (89%) and HS (19%) states of Fe(II)	23Y021
Fe-57 14.40 keV Transition: Inorganic Halides						
xx	hybrid composites of high entropy perovskites $CsMBr_3$ (M=Pb, Fe, Co, Ni, Mn) with Cs/M=1:1, 1:2, and 1:3	v	--	--	claimed the presence of LS and HS states of Fe	24C003
Fe-57 14.40 keV Transition: Inorganic Oxides						
Rh(IS/α-Fe)	amorphous SiO_2 implanted with 60 keV ^{57}Fe	300	--	--	identified sextet components (B_{hf}=33.5 T, 31.1T and 29.1 T) consistent with the precipitation of metallic α-Fe nanoclusters, and doublets, assigned to Fe^{2+} and Fe^{3+} species	24B008
Rh(IS/α-Fe)	$BaFe_{11.75}Zn_{0.25}O_{19}$ ferrite before and after magnetic pulse processing	300	--	--	both averaged B_{hf} and QS decrease with increasing the time of magnetic pulse processing	23S090
Rh(IS/α-Fe)	$BaFe_{12-x}Al_xO_{19}$ (*x*=0, 0.5, 1.0, 1.5)	300	--	--	identified 5 sextets assigned to the sites: three octahedral (2a, 4f_2, and 12 k), one tetrahedral (4f_1) and one trigonal bipyramidal (2b)	24B006
Rh(IS/Fe)	$BaTi_{1-x}Fe_xO_3$(*x*=0.02)	300	--	--	identified a doublet and detected a presence of 2 minor impurity sextets attributed to the impurity ordering of both FM and AFM types among Fe^{3+}	24B002

Source	Absorber	Temp	IS	QS	Comments	Code
Rh(IS/α-Fe)	bentonites and montmorillonites from Georgia and Wyoming, USA, and bentonites from Czech Republic, Italy, India and Greece	300	--	--	determined the structural localization. hyperfine parameters and the extent of reduction of Fe, and distinguished 3 groups of bentonites, based on the sulfide oxidation capacity	23H035
Rh(IS/α-Fe)	biogenic ferrihydrite manoparticles before and after low-temperature annealing at 150°C in air for 24 h	v	--	--	sites of Fe1, Fe2 and Fe3 are identified with 3 doublets at 300 K and with three sextets at 4.2 K	23K057
Rh(IS/α-Fe)	CE-5 lunar soil CE5C0600	300	--	--	applied a fitting model of a sextet (alpha-Fe, 2.5%) and three Fe^{2+} doublets: D1 (ilmenite, 9%), D2 (pyroxene M1+olivine, 33%) and D3 (pyroxene M2+glass, 55%)	24Q001
Rh(IS/sodium nitroprusside)	Ceramic Brick Based on Power Plant Waste (80% interstitial clay + 20% iron-bearing power plant slag)	300	--	--	identified presence of magnetite in combination with hematite and fayalite	23A041
Rh(IS/α-Fe)	$Co_{1-x}Zn_xFe_2O_4$ (x=0.0-0.56) ferrites synthesized by sol-gel autocombustion	v	--	--	spectra are a combination of broad sextet, and a dominant paramagnetic doublet with QS of 0.70 – 0.84 mm/s, and the doublet area range between 20 – 50%	23K062
Rh(IS/α-Fe)	$CoFe_2O_4$	80	--	--	reviewed different approaches to deconvolute the spectrum: two-component fit, three-component fit, six-component fit	24B009
Rh(IS/α-Fe)	core—shell nanoparticles composed of the Fe_3O_4 core and a mixed shell built of iron and silicon glycerolates	295	--	--	demonstrated that the Fe : Si atomic ratio in the mixed shell of ISG-MNPs is about 1 : 1	23K061
Rh(IS/α-Fe)	crystalline SiO_2 implanted with 60 keV ^{57}Fe	300	--	--	identified high-B_{hf} sextet components (B_{hf}=52.7 T and 52.3 T) consistent with the precipitation of α-Fe_2O_3 and a doublet, assigned to Fe^{3+} species	24B008
Rh(IS/α-Fe)	destinezite $Fe_2(PO_4)(SO_4)(OH)\cdot 6H_2O$ from Hloubětí*n* (Czech Republic)	v	0.41	0.21	identified a stronger broadening within the doublet of the left-hand Lorentzian compared to a narrower right-hand Loretzian for both 78 K and 300 K	23G046
Rh(IS/α-Fe)	disordered gel with a crosslinked structure of $CaO–Fe_2O_3–Al_2O_3–SiO_2–H_2O$	300	--	--	identified two kinds of octahedral Fe^{3+} : the distorted one (modifier), and more symmetric (a layer former)	23F016
Cr(IS/α-Fe)	$Fe_{3-x}Mn_xO_4$ $0.00 < x < 0.25$ nanoparticles synthesized via co-precipitation method	300	--	--	observed no spm-relaxation and suggested that the ferrite particle size is above 4.2-4.6 nm	23D036
Rh(IS/α-Fe)	goethite nanoparticles and Zn-doped goethite nanoparticles (5, 10, and 20% at.)	300	--	--	identified Fe in alpha-(Fe, Zn)OOH goethite nanoparticles and impurity phases of non-stoichiometric zinc ferrite (31% for 20% of Z), and a small fraction of fine maghemite	24B004
Rh(IS/α-Fe)	Hm/C_y@C-900 and Hm/TCA@C-900 electrocatalysts	300	--	--	identified the actual iron components to be the phases of Fe_3C, FeS_x, Fe_3O_4, and metallic alpha-Fe nanoparticles	23L055
Rh(IS/α-Fe)	hollow α-Fe_2O_3 microspheres produced by spray pyrolysis	v	--	--	identified major (86%) and minor (14%) sextets assigned to bulk (B_{hf}=51.4 T) and surface (B_{hf}=49 T)	23D034
Rh(IS/α-Fe)	iron oxide nanoparticles and Fe_3O_4-$\gamma Fe_2O_3/(C_{60}Pd_3)_n$ composites	300	--	--	identified under magnetic field of 1.3 T three components assigned to A and B sites of maghemite and a surface	23W028
xx(IS/α-Fe)	iron-rich cementitious materials, such as brownmillerite $Ca_2Al_xFe_{2-x}O_5$, augite Ca,Na)(Mg,Fe,Al,Ti)(Si,Al)$_2O_6$, phyllosilicates, jarosites, etc.	v	--	--	reviewed Mössbauer spectroscopy among other methods required to apply them in the field of cementitious materials	24B007
Rh(IS/α-Fe)	$LiFeCr_4O_8$	v	--	--	determined the temperature dependence of hyperfine parameters showing the ferrimagnetic transition at $T_N \sim 94$ K, the spin-gap transition at $T_{SG} \sim 50$ K, and the magnetostructural transition at $T_{MS} \sim 19$ K	23Z042
Rh(IS/α-Fe)	magnetic nanoparticles of $Ni_{0.4}Zn_{0.6}Fe_2O_4$, $Ni_{0.4}Zn_{0.6}Ce_{0.1}Fe_{1.9}O_4$, $Ni_{0.6}Zn_{0.4}Ce_{0.1}Fe_{1.9}O_4$, and $Ni_{0.5}Zn_{0.5}Ce_{0.1}Fe_{1.9}O_4$	300	--	--	identified A and B sextets and spm-doublets; large QS indicate high asymmetry at both sites A and B	24D002
Rh(IS/α-Fe)	$MgFe_2O_4$ and $Mg(Fe_{0.8}Ga_{0.2})_2O_4$ prepared by auto-combustion method	v	--	--	performed measurements at 776 K and at 14 K and obtained the ratios of the intensities of the partial for two iron positions, I(FeA)/I(FeB), ~0.72 and ~0.89 for $MgFe_2O_4$ and $Mg(Fe_{0.8}Ga_{0.2})_2O_4$, respectively	23G045
Rh(IS/α-Fe)	multiferroics $Bi_{1-x}Sr_xFeO_{3-y}$ (x=0, 0.05, and 0.10)	300	--	--	identified three P(B_{hf}) distributions, each described within the model of cycloid spatial anharmonic spin modulation	23P040

Source	Absorber	Temp	IS	QS	Comments	Code
Rh(IS/α-Fe)	$M_xCo_{1-x}Fe_2O_4$ (M^{2+}=Ni^{2+}, Zn^{2+})	v	--	--	identified A and B sites; determined the cation distribution and observed a small Zn^{2+} quantity in Oh-sites.	24B005
Rh(IS/α-Fe)	Na_2FePO_4F cathode for aqueous zinc-ion batteries at three states (pristine, 1st charge, and 1st discharge	v	--	--	identified the Fe^{2+} and Fe^{3+} doublets, and confirmed the Fe^{2+}/Fe^{3+} redox activity	23S088
Rh(IS/α-Fe)	nanocomposites synthesized from Fe ablated in acetone, Fe ablated in toluene, and Fe ablated in heated toluene	293	--	--	identified γ-Fe_2O_3 phase (100%) for acetone, and γ-Fe_2O_3 (20%) and austenite (26%) and Fe_3C (40%) and amorphous Fe (14%) for toluene	24D004
Rh(IS/α-Fe)	Nanoparticles of $MnFe_2O_4$,Fe_3O_4,and $CoFeO_4$ coated with PLLA-PVA capsules	v	--	--	identified sextets of A and B sites for $MnFe_2O_4$, and $CoFeO_4$, and A, B2, B2 sites for Fe_3O_4	23A040
Rh(IS/α-Fe)	Nd_Pr_Fe_B machining wastes from two different machining processes (diamond cutting and grinding)	300	--	--	identified $R_2Fe_{14}B$; the hyperfine fields of the $R_2Fe_{14}B$ (R=rare-earth element) decrease in the following order: $8j_2 > 16k_2 > 16k_1 > 4e > 8j_1 > 4c$	23B061
Rh(IS/α-Fe)	$Ni_{0.5}Zn_{0.5}R_{0.02}Fe_{1.98}O_4$ for R=Ce and Gd sintered at 500℃	5	--	--	observed by application external field of 5 T the suppression of 2nd and 5th lines for both A and B sextets	23P042
Rh(IS/α-Fe)	$Ni_{0.65}Zn_{0.35}Al_xFe_{2-x}O_4$ (x =0.0, 0.5, and 1)	300	--	--	B_{hf} decreases from 37.4 to 31.4 T as x increases from 0 to 1	23U007
Rh(IS/α-Fe)	of iron oxide (α-Fe_2O_3) nanoparticles functionalized with chitosan synthesized by hydrothermal method	300	--	--	observed spectra modelled with a doublet and 3 sextets or a sextet with the asymmetric line broadening assigned to a mixed slow-fast relaxation	23D035
Rh(IS/α-Fe)	oxides‐based red pigments in the ancient Gaya region, South Korea	295	--	--	identified sextets of A and B sites of magnetite, phase of α-Fe_2O_3 (hematite) and Fe^{3+} doublets D1(spm-Fe_2O_3), D2 (kaolin), D3(clay mineral), D6(clinochlore), and two other doublets assigned to Fe^{2+} in clinochlore	23M054
Rh(IS/α-Fe)	paddy soil from the Ubon Ratchathani Rice Research Center in Thailand before and after incubation with	5	--	--	identified mainly ferrihydrite and lepidocrocite; observed that ferrihydrite was less stable during mineral transformation and reductive dissolution, compared to lepidocrocite	23S092
SMS at ID18, ESRF	perovskites $Fe_{0.5}Mg_{0.5}Al_{0.5}Si_{0.5}O_3$ and $FeMg_{0.5}Si_{0.5}O_3$ up to 95GPa	300	--	--	above approximately 12 GPa $FeMg_{0.5}Si_{0.5}O_3$ transforms into a new silicate double perovskite having two individual octahedral sites: one occupied by Si only, and the other by iron and magnesium	23K055
Rh	phosphate-free schwertmannite $Fe_8O_8(OH)_{8-2x}(SO_4)_x$ and phosphate-sorbed at pH 3, pH 6, and pH 8	300	--	--	from the relative fractions of collapsed sextet and doublet detected an increase in crystallinity with pH, and a decrease in crystallinity after reaction with phosphate	24A004
Cr(IS/α-Fe)	porous carbon material before and after laser irradiation and aging	300	--	--	identified Fe in compounds OF $FeO_n{\cdot}H_2O$ and β-FeOOH	23B063
Rh(IS/α-Fe)	pyrochlore-like layered $Y_{1.85}Mg_{0.15}FeTaO_7$ and $Y_2Fe_{0.7}Mg_{0.3}TaO_7$	300	--	--	observed the existence of magnetic ordering at room temperature in one magnetic sublattice (B_{hf}=45.6 to 51.8 T) and paramagnetic doublets from other two sublattices assigned to Fe^{3+} and $Fe(3+delta)^+$	23E012
Rh(IS/α-Fe)	Sr_2FeNbO_6-delta	v	--	--	identified at 7K two types of magnetic structures that differ in the length and strength of antiferromagnetic correlations; Fe1 (3+) and Fe2 (3+) centers account for 61% and 39% of the total area	23P037
Rh(IS/α-Fe)	synthetic fayalite Fe_2SiO_4	v	--	--	reviewed powder and single crystal Mössbauer spectroscopy studies on synthetic fayalites	23T019
Rh(IS/α-Fe)	synthetic Mg-rich and Na, Si-rich majorites synthesized at 18–25 GPa and 1000 °C	300	--	--	reviewed the applications of Mössbauer spectroscopy for determination of the ratio of $Fe^{3+}/\Sigma Fe$ and determined the changes of $Fe^{3+}/\Sigma Fe$ with pressure	23S070
Rh(IS/α-Fe)	thin layers of $CuFeO_2$ prepared by radio frequency magnetron sputtering, and by reactive high-power impulse magnetron sputtering combined with electron cyclotron wave resonance plasma (HiPIMS-ECWR)	300	--	--	identified delafossite $CuFeO_2$ after magnetron sputtering and additionally iron oxides (magnetite, maghemite) after HiPIMS-ECWR	23P039
Rh(IS/α-Fe)	trachybasalt porphyrite from the Karabulak site of the Gavasay deposit	300	--	--	identified sextets and doublets assigned to magnetite, titanomagnetite and a glass, and estimated the estimate the Fe^{3+}/Fe(total) ratio	23K060
Rh(IS/α-Fe)	$Y_{2.5}Ce_{0.5}Fe_{2.5}Ga_{2.5}O_{12}$ before and after annealing in vacuum, and in vacuum and then in air	298	--	--	observed ratio of iron cations in tetrahedral and octahedral sites((Fe(Td)/Fe(Oh)) deviates from the 3 : 2, indicating the preference of Ga atoms to Td sites	23T021

Source	Absorber	Temp	IS	QS	Comments	Code
Rh(IS/α-Fe)	$Y_3Fe_{5-x}Al_xO_{12}$	300	--	--	identified three subspectra for the octahedral environment of Fe^{3+} and four subspectra for the tetrahedral environment of Fe^{3+}	23K059
Rh(IS/α-Fe)	$Zn_{0.5}Ni_{0.5}Fe_2O_4$ nanoparticles	300	--	--	identified a Zeeman sextet assigned to Fe^{3+} in B site with a hyperfine field value of 37.8 T	24D003
Rh(IS/α-Fe)	$Zn_xFe_{3-x}O_4$ (for x=0, 0.25, 0.5, 0.75 and 1.0) functionalized with polyacrylic acid $Zn_xFe_{3-x}O_4$@PAA	300	--	--	modelled the spectra with the sextet subspectra of A, B1, B2, B3 and B4 for x=0; A, B1, B2 and a surface-like collapsed sextet for x = 0.25; A, B1, surface-collapsed S, and doublet D for x=0.5; A+B, surface-collapsed S, and doublet D for x=0.75; and doublets D1,D2 and impurity(Fe_2O_3) sextet for x=1	23K056
Rh(IS/α-Fe)	γ-Fe_2O_3 and γ-Fe_2O_3/SiO_2	300	--	--	coating of nanoparticles leads to a change in the fraction of the superparamagnetic doublet and relaxational component	23S091
Rh(IS/α-Fe)	γ-iron oxide nanoparticles and carboxylate (valerate, butyrate, formate and acetate) precursors before pyrolysis	v	--	--	explained the <B_{hf}> shift from 482 kOe (initial iron valerate) to 460 kOe (initial iron butyrate) by the particle size γ-iron oxide of dependence on precursor	23S093
Fe-57 14.40 keV Transition: Inorganic Sulfides						
Rh(IS/α-Fe)	Hm/C_y@C-900 and Hm/TCA@C-900 electrocatalysts	300	--	--	identified the actual iron components to be the phases of Fe_3C, FeS_x, Fe_3O_4, and metallic alpha-Fe nanoparticles	23L055
Rh(IS/α-Fe)	initial and leached sulfide minerals from the Southwest Indian Ridge	300	--	--	identified the phases of pyrite, sphalerite, hydrous ferric oxides and chalcopyrite	23H038
Fe-57 14.40 keV Transition: Inorganic Sulphates						
Rh(IS/α-Fe)	destinezite $Fe_2(PO_4)(SO_4)(OH)\cdot 6H_2O$ from Hloubětí*n* (Czech Republic)	v	0.41	0.21	identified a stronger broadening within the doublet of the left-hand Lorentzian compared to a narrower right-hand Loretzian for both 78 K and 300 K	23G046
Rh	phosphate-free schwertmannite $Fe_8O_8(OH)_{8-2x}(SO_4)_x$ and phosphate-sorbed at pH 3, pH 6, and pH 8	300	--	--	from the relative fractions of collapsed sextet and doublet detected an increase in crystallinity with pH, and a decrease in crystallinity after reaction with phosphate	24A004
Fe-57 14.40 keV Transition: Irradiation Experiments						
Rh(IS/α-Fe)	amorphous SiO_2 implanted with 60 keV ^{57}Fe	300	--	--	identified sextet components (B_{hf}=3.5 T, 31.1T and 29.1 T) consistent with the precipitation of metallic α-Fe nanoclusters, and doublets, assigned to Fe^{2+} and Fe^{3+} species	24B008
Rh(IS/α-Fe)	$BaFe_{11.75}Zn_{0.25}O_{19}$ ferrite before and after magnetic pulse processing	300	--	--	both averaged B_{hf} and QS decrease with increasing the time of magnetic pulse processing	23S090
Rh(IS/α-Fe)	CE-5 lunar soil CE5C0600	300	--	--	applied a fitting model of a sextet (alpha-Fe, 2.5%) and three Fe^{2+} doublets: D1 (ilmenite, 9%), D2 (pyroxene M1+olivine, 33%) and D3 (pyroxene M2+glass, 55%)	24Q001
Rh(IS/α-Fe)	crystalline SiO_2 implanted with 60 keV ^{57}Fe	300	--	--	identified high-B_{hf} sextet components (B_{hf}=52.7 T and 52.3 T) consistent with the precipitation of α-Fe_2O_3 and a doublet, assigned to Fe^{3+} species	24B008
Rh(IS/α-Fe)	of iron oxide (α-Fe_2O_3) nanoparticles functionalized with chitosan synthesized by hydrothermal method	300	--	--	observed spectra modelled with a doublet and 3 sextets or a sextet with the asymmetric line broadening assigned to a mixed slow-fast relaxation	23D035
Fe-57 14.40 keV Transition: Metals and Alloys						
Rh(IS/α-Fe)	30 μm α-iron foil	v	--	--	optimized with measurements from a laser Doppler vibrometer the miniaturized piezoelectric Mössbauer spectrometer based on a piezoelectric actuator	23G044
a synchrotron source of third generation	a thin-film planar cavity implanted in the Mössbauer nuclei Pt (0.5 nm) /C (20.8 nm) /^{56}Fe (0.6 nm) /C (19.6 nm) / Pt (2.5 nm), Pd (3.5 nm) /C (20.8 nm) /^{56}Fe (0.6 nm) / C (19.6 nm) /Pd (2.5 nm), and Pd (4 nm) /C (18 nm) /^{56}Fe (1.2 nm) /C (18 nm) /Pd (14 nm)	v	--	--	replacing ^{56}Fe with ^{57}Fe (abundance=100%), calculated by the CONUSS package the reflectivity spectra and reviewed the X-ray quantum optics with Mössbauer nuclei embedded in thin-film cavities	23L056
Rh(IS/α-Fe)	$Al_{79}Ni_5Fe_5Y_{11}$ and $Al_{79}Ni_{11}Fe_5Y_5$ alloys	v	--	--	performed a fit with 2 QS distributions and assigned Fe with higher QS to mainly aluminium and yttrium surrounding, and Fe with lower QS to iron atoms surrounded mainly by aluminium and nickel atoms	23M056
Rh(IS/α-Fe)	CE-5 lunar soil CE5C0600	300	--	--	applied a fitting model of a sextet (alpha-Fe, 2.5%) and three Fe^{2+} doublets: D1 (ilmenite, 9%), D2 (pyroxene M1+olivine, 33%) and D3 (pyroxene M2+glass, 55%)	24Q001
Rh(IS/α-Fe)	Fe	v	--	--	developed an advanced velocity modulator for a portable Mössbauer spectrometer	23Y022

Source	Absorber	Temp	IS	QS	Comments	Code
Rh(IS/α-Fe)	$Fe_{0.258}Ga_{0.742}$	300	--	--	observed the existence of 2 doublets assigned to Fe at two dierent environments: pristine ($FeGa_3$) and Fe antisite	23R027
Rh(IS/α-Fe)	Heusler alloy Fe_2RuGe	v	--	--	identified three Fe sites with the relative absorption areas of 55%, 23%, and 22% for the three sites Fe-4b, Fe-4c, and Fe-4d, with $<B_{hf}>$ at 300 K of 30.6, 23.3, and 21.8 T	23C034
Rh(IS/α-Fe)	Kagomé Metal (Zr,Ta)Fe^2 annealed at different temperatures (1473K and 1073K)	300	--	--	identified 4 magnetically inequivalent Fe sites (6h, 2a and two 16d) and determined the ratio and hyperfine field of each Fe atoms	23C033
Rh(IS/α-Fe)	melt-spun Fe–Si–B amorphous alloy ribbons ($Fe_{78}Si_9B_{13}$)	300	--	--	identified a preferred spin orientation: the majority of magnetic aligned parallel to the surface of the ribbon	23A042
Rh(IS/α-Fe)	metal-nanocomposites Fe-Mn-Ni-C synthesized by mechanical milling	v	--	--	identified magnetic ferrite, austenite (paramagnetic and ferromagnetic), and cementite (both paramagnetic and ferromagnetic))	23U006
Rh(IS/α-Fe)	nanocomposites synthesized from Fe ablated in acetone, Fe ablated in toluene, and Fe ablated in heated toluene	293	--	--	identified γ-Fe_2O_3 phase (100%) for acetone, and γ-Fe_2O_3 (20%) and austenite (26%) and Fe_3C (40%) and amorphous Fe (14%) for toluene	24D004
xx(IS/α-Fe)	quasi-binary alloys with Laves structure	v	--	--	this is an erratum to an early published article 'The Creation of Complex Multi- Component Models of Mössbauer Spectra...'	23M057
Fe-57 14.40 keV Transition: Miscellaneous Experiments						
Rh(IS/α-Fe)	amino-ferrocene powder and amino-ferrocene-based nanoclusters on a graphene oxide nanosheet	v	--	--	Fe ion changed from a non-magnetic S=0 state to a S=5/2 high-spin state by charge transfer when assembled by on-surface chemical reaction on a GO nanosheet	23S096
a synchrotron or free-electron laser	ensembles of nuclei embedded in *x*-ray waveguides	300	--	--	explored a method to detect an excitation of nuclear ensembles beyond the low-excitation regime	23W026
xx	hybrid composites of high entropy perovskites $CsMBr_3$ (M=Pb, Fe, Co, Ni, Mn) with Cs/M=1:1, 1:2, and 1:3	v	--	--	claimed the presence of LS and HS states of Fe	24C003
Rh(IS/α-Fe)	iron polyhydrides FeH_x synthesized with ^{57}Fe at 178 and 195 GPa	300	--	--	reviewed the previous Mössbauer data showing that the hydride phase is magnetically ordered according to the Mössbauer spectroscopy data	23G047
Rh(IS/α-Fe)	magnetic nanoparticles of $Ni_{0.4}Zn_{0.6}Fe_2O_4$, $Ni_{0.4}Zn_{0.6}Ce_{0.1}Fe_{1.9}O_4$, $Ni_{0.6}Zn_{0.4}Ce_{0.1}Fe_{1.9}O_4$, and $Ni_{0.5}Zn_{0.5}Ce_{0.1}Fe_{1.9}O_4$	300	--	--	identified A and B sextets and spm-doublets; large QS indicate high asymmetry at both sites A and B	24D002
Rh	phosphate-free schwertmannite $Fe_8O_8(OH)_{8-2x}(SO_4)_x$ and phosphate-sorbed at pH 3, pH 6, and pH 8	300	--	--	from the relative fractions of collapsed sextet and doublet detected an increase in crystallinity with pH, and a decrease in crystallinity after reaction with phosphate	24A004
Rh(IS/α-Fe)	γ-iron oxide nanoparticles and carboxylate (valerate, butyrate, formate and acetate) precursors before pyrolysis	v	--	--	explained the $<B_{hf}>$ shift from 482 kOe (initial iron valerate) to 460 kOe (initial iron butyrate) by the particle size γ-iron oxide of dependence on precursor	23S093
Fe-57 14.40 keV Transition: Miscellaneous Inorganic Compounds						
Rh(IS/α-Fe)	amino-ferrocene powder and amino-ferrocene-based nanoclusters on a graphene oxide nanosheet	v	--	--	Fe ion changed from a non-magnetic S = 0 state to a S=5/2 high-spin state by charge transfer when assembled by on-surface chemical reaction on a GO nanosheet	23S096
Rh(IS/α-Fe)	core—shell nanoparticles composed of the Fe_3O_4 core and a mixed shell built of iron and silicon glycerolates	295	--	--	demonstrated that the Fe:Si atomic ratio in the mixed shell of ISG-MNPs is about 1:1	23K061
a synchrotron or free-electron laser	ensembles of nuclei embedded in *x*-ray waveguides	300	--	--	explored a method to detect an excitation of nuclear ensembles beyond the low-excitation regime	23W026
xx	hybrid composites of high entropy perovskites $CsMBr_3$ (M=Pb, Fe, Co, Ni, Mn) with Cs/M=1:1, 1:2, and 1:3	v	--	--	claimed the presence of LS and HS states of Fe	24C003
Rh(IS/α-Fe)	iron polyhydrides FeH_x synthesized with ^{57}Fe at 178 and 195 GPa	300	--	--	reviewed the previous Mössbauer data showing that the hydride phase is magnetically ordered according to the Mössbauer spectroscopy data	23G047
xx(IS/α-Fe)	iron-rich cementitious materials, such as brownmillerite $Ca_2Al_xFe_{2-x}O_5$, augite $Ca,Na)(Mg,Fe,Al,Ti)(Si,Al)_2O_6$, phyllosilicates, jarosites, etc.	v	--	--	reviewed Mössbauer spectroscopy among other methods required to apply them in the field of cementitious materials	24B007

Source	Absorber	Temp	IS	QS	Comments	Code
Rh(IS/α-Fe)	melt-spun Fe–Si–B amorphous alloy ribbons ($Fe_{78}Si_9B_{13}$)	300	--	--	identified a preferred spin orientation: the majority of magnetic aligned parallel to the surface of the ribbon	23A042
Rh(IS/α-Fe)	metal-nanocomposites Fe-Mn-Ni-C synthesized by mechanical milling	v	--	--	identified magnetic ferrite, austenite (paramagnetic and ferromagnetic), and cementite (both paramagnetic and ferromagnetic))	23U006
Rh(IS/α-Fe)	MOF_{74} and Fe-containing metal-organic frameworks	v	--	--	proposed a method for calculation of the temperature dependence of the quadrupole splitting compounds	23P041
Rh(IS/α-Fe)	nanocomposites synthesized from Fe ablated in acetone, Fe ablated in toluene, and Fe ablated in heated toluene	293	--	--	identified γ-Fe_2O_3 phase (100%) for acetone, and γ-Fe_2O_3 (20%) and austenite (26%) and Fe_3C (40%) and amorphous Fe (14%) for toluene	24D004
Rh	phosphate-free schwertmannite $Fe_8O_8(OH)_{8-2x}(SO_4)_x$ and phosphate-sorbed at pH 3, pH 6, and pH 8	300	--	--	from the relative fractions of collapsed sextet and doublet detected an increase in crystallinity with pH, and a decrease in crystallinity after reaction with phosphate	24A004
Rh(IS/α-Fe)	γ-iron oxide nanoparticles and carboxylate (valerate, butyrate, formate and acetate) precursors before pyrolysis	v	--	--	explained the <B_{hf}> shift from 482 kOe (initial iron valerate) to 460 kOe (initial iron butyrate) by the particle size γ-iron oxide of dependence on precursor	23S093
Fe-57 14.40 keV Transition: Organic Compounds						
Rh(IS/α-Fe)	(2,2′-bipyridyl)-$FeF_3{\cdot}2H_2O$	297	0.39	0.94	identified the high spin state and confirmed the high sample quality	24W002
Rh(IS/α-Fe)	(L2)$FeCH_3$ quinoline pyridine(imine) iron complex (QPI=N-(2,6-dimethylphenyl)-1-(6-(quinolin-2-yl)-pyridin-2-yl)ethan-1-imine)	80	0.53	1.27	identified the antiferromagnetic coupling of HS Fe(II) to a singly reduced (QPI1−) ligand with a total spin of (S=3/2)	23D033
Rh(IS/α-Fe)	2+, 3+ and 4+ charge states of the heterotrimetallic cyanido–metal-bridged complexes, trans-[Cp(dppe)Fe-CN-Ru(MeOpy)$_4$-NC-Fe(dppe)Cp][X]$_n$ (n=2, 3, or 4); X=PF_6 or BF_4) (Cp=cyclopentadiene, dppe=1,2-bis(diphenylphosphino)ethane)	v	--	--	in the one-electron oxidation compounds (3+ state) the charge is delocalized all along the trimetal backbone Fe–Ru–Fe	23Z043
Rh(IS/α-Fe)	2+, 3+ and 4+ oxidation compounds of the heterotrimetallic cyanido–metal-bridged complexes, [Cp*(dppe)Fe-CN-Ru(MeOpy)$_4$-NC-Fe(dppe)Cp*][X]$_n$; Cp*= 1,2,3,4,5-pentamethylcyclopentadiene; n=2, 3, or 4; X=PF_6 or BF_4)	v	--	--	in the one-electron oxidation compounds (3+ state) the charge is delocalized between the two metal parts Fe–Ru	23Z043
Rh(IS/α-Fe)	amino-ferrocene powder and amino-ferrocene-based nanoclusters on a graphene oxide nanosheet	v	--	--	Fe ion changed from a non-magnetic S = 0 state to a S = 5/2 high-spin state by charge transfer when assembled by on-surface chemical reaction on a GO nanosheet	23S096
Rh(IS/α-Fe)	complexes {FeDEsP-NO}$_7$ and {FeTEsP-NO}$_7$ before adding cobaltocene, and after adding cobaltocene	90	--	--	the addition of cobaltocene resulted in the appearance of additional doublets assigned to {FeDEsP-NO}$_8$ and {FeTEsP-NO}$_8$	23S085
Rh(IS/α-Fe)	core—shell nanoparticles composed of the Fe_3O_4 core and a mixed shell built of iron and silicon glycerolates	295	--	--	demonstrated that the Fe : Si atomic ratio in the mixed shell of ISG-MNPs is about 1 : 1	23K061
Rh(IS/α-Fe)	Fe(4-ethynylpyrdine)$_2$[Fe(CN)$_5$NO]	v	--	--	identified 2 Fe(II) LS subspectra at 5 K and the Fe(II)LS + Fe(II) HS subspectra at 295 K	23S087
Rh(IS/α-Fe)	Fe(Py$_z$)[Fe-(CN)$_5$NO] before and after insertion the guest species (benzene/toluene or furan/thiophene)	5	--	--	identified the Fe(II) LS and HS doublets; the guest-host interaction is favorable to the SCO for benzene and toluene and unfavorable for furan and thiophene	23S086
Rh(IS/α-Fe)	ferrous protein, after incubation with $Na_2S_2O_4$, and Mb-cIII, trapped after further incubation	300	--	--	identified the low-spin iron (II) species with an isomer shift (δ) of 0.47mm/s and a quadrupole splitting (|ΔE_Q|) of 1.00 mm/s before and HS Fe(II) after carbene moiety is transferred to a ring nitrogen atom of the porphyrin cofactor (δ=0.97mm/s and |ΔE_Q|=4.00mm)	23N028
Rh(IS/Fe)	iron (II)-triazole complex [Fe(atrz)$_3$](2 ns)$_2$	293	0.278	0.074	identified presence of a single clear doublet signal assigned to Fe^{II} in the LS state	24B003

Source	Absorber	Temp	IS	QS	Comments	Code
Rh(IS/α-Fe)	iron(III)-peroxo complex bearing an N-tetramethylated cyclam ligand, $[Fe^{III}(O_2)(12\text{-TMC})]^+$	4.2	0.53	--	demonstrated paramagnetic relaxation of a single species having an S=5/2 spin state a small axial zero-field splitting (D=−1 cm^{-1}), a large rhombic zero-field splitting (E/D=0.31), and a close-to-isotropic A tensor ([−20.0, −20.0, −21.2] T)	23Y023
Rh(IS/α-Fe)	MOF_{74} and Fe-containing metal-organic frameworks	v	--	--	proposed a method for calculation of the temperature dependence of the quadrupole splitting compounds	23P041
Rh(IS/α-Fe)	neutral tetranitrosyl iron complex $\{[Fe(H_2O)_4]^{2+}[FeR_2(NO)_2]_2^{2-}\}\cdot 4H_2O$ with R=5-(3-pyridyl) -4H-1,2,4-triazole-3-thiolyls	295	--	--	identified two doublets with intensity ratio of 2:1, assigned to Fe(I)LS (major) and Fe(II)LS (minor)	23S095
Rh(IS/α-Fe)	of iron oxide (α-Fe_2O_3) nanoparticles functionalized with chitosan synthesized by hydrothermal method	300	--	--	observed spectra modelled with a doublet and 3 sextets or a sextet with the asymmetric line broadening assigned to a mixed slow-fast relaxation	23D035
Rh(IS/α-Fe)	polymer $\{Fe(DPPE)_2[Ag(CN)_2]_2\}\cdot 2EtOH$ with a luminescent ligand DPPE=1,1-diphenyl-2,2-di(4-py ridylbiphenyl)ethylene	40	--	--	identified the doublet subspectra for the LS (89%) and HS (19%) states of Fe(II)	23Y021
Rh(IS/α-Fe)	resorcinol–formaldehyde hybrid aerogels with ferrocene subunit fragments	78	--	--	identified low-spin iron Fe^{2+} cations (d6 in Fe1) for major subspectrum (QS=2.38 mm/s) and a relaxational behavior for minor (Fe2)	23P043
Fe-57 14.40 keV Transition: Terrestrial and Extraterrestrial Minerals						
Rh(IS/α-Fe)	bentonites and montmorillonites from Georgia and Wyoming, USA, and bentonites from Czech Republic, Italy, India and Greece	300	--	--	determined the structural localization. hyperfine parameters and the extent of reduction of Fe, and distinguished 3 groups of bentonites, based on the sulfide oxidation capacity	23H035
Rh(IS/α-Fe)	CE-5 lunar soil CE5C0600	300	--	--	applied a fitting model of a sextet (alpha-Fe, 2.5%) and three Fe^{2+} doublets: D1 (ilmenite, 9%), D2 (pyroxene M1+olivine, 33%) and D3 (pyroxene M2+glass, 55%)	24Q001
Rh(IS/sodium nitroprusside)	Ceramic Brick Based on Power Plant Waste (80% interstitial clay + 20% iron-bearing power plant slag)	300	--	--	identified presence of magnetite in combination with hematite and fayalite	23A041
Rh(IS/α-Fe)	destinezite $Fe_2(PO_4)(SO_4)(OH)\cdot 6H_2O$ from Hloubětín (Czech Republic)	v	0.41	0.21	identified a stronger broadening within the doublet of the left-hand Lorentzian compared to a narrower right-hand Loretzian for both 78 K and 300 K	23G046
Rh(IS/α-Fe)	initial and leached sulfide minerals from the Southwest Indian Ridge	300	--	--	identified the phases of pyrite, sphalerite, hydrous ferric oxides and chalcopyrite	23H038
xx(IS/α-Fe)	iron-rich cementitious materials, such as brownmillerite $Ca_2Al_xFe_{2-x}O_5$, augite $Ca,Na)(Mg,Fe,Al,Ti)(Si,Al)_2O_6$, phyllosilicates, jarosites, etc.	v	--	--	reviewed Mössbauer spectroscopy among other methods required to apply them in the field of cementitious materials	24B007
Rh(IS/α-Fe)	Nd-Pr-Fe-B machining wastes from two different machining processes (diamond cutting and grinding)	300	--	--	identified $R_2Fe_{14}B$; the hyperfine fields of the $R_2Fe_{14}B$ (R=rare-earth element) decrease in the following order: $8j_2 > 16k_2 > 16k_1 > 4e > 8j_1 > 4c$	23B061
Rh(IS/α-Fe)	oxides-based red pigments in the ancient Gaya region, South Korea	295	--	--	identified sextets of A and B sites of magnetite, phase of α-Fe_2O_3 (hematite) and Fe^{3+} doublets D1(spm-Fe_2O_3), D2 (kaolin), D3(clay mineral), D6(clinochlore), and two other doublets assigned to Fe^{2+} in clinochlore	23M054
Rh(IS/α-Fe)	paddy soil from the Ubon Ratchathani Rice Research Center in Thailand before and after incubation with	5	--	--	identified mainly ferrihydrite and lepidocrocite; observed that ferrihydrite was less stable during mineral transformation and reductive dissolution, compared to lepidocrocite	23S092
SMS at ID18, ESRF	perovskites $Fe_{0.5}Mg_{0.5}Al_{0.5}Si_{0.5}O_3$ and $FeMg_{0.5}Si_{0.5}O_3$ up to 95GPa	300	--	--	above approximately 12 GPa $FeMg_{0.5}Si_{0.5}O_3$ transforms into a new silicate double perovskite having two individual octahedral sites: one occupied by Si only, and the other by iron and magnesium	23K055
Rh(IS/α-Fe)	synthetic Mg-rich and Na, Si-rich majorites synthesized at 18–25 GPa and 1000 °C	300	--	--	reviewed the applications of Mössbauer spectroscopy for determination of the ratio of $Fe^{3+}/\Sigma Fe$ and determined the changes of $Fe^{3+}/\Sigma Fe$ with pressure	23S070
Rh(IS/α-Fe)	trachybasalt porphyrite from the Karabulak site of the Gavasay deposit	300	--	--	identified sextets and doublets assigned to magnetite, titanomagnetite and a glass, and estimated the estimate the Fe^{3+}/Fe(total) ratio	23K060

Source	Absorber	Temp	IS	QS	Comments	Code
Ir-193 73.00 keV Transition						
Dynamics Beamline P01 (PETRA III, DESY, Hamburg	iridium(I) complex $[IrCl(COD)]_2$ with COD being cycloocta-1,5-diene (of Di-μ-chlorobis[(1,2,5,6-η)-1,5-cyclooctadiene)	10	0.87	3.82	obtained IS and QS from ^{193}Ir-NFS data with the CONUSS software by Alexeev's method	23H036
Sb-121 37.20 keV Transition						
$Ca^{121m}SnO_3$	Ni_2SbTe_2 and $Ni_{2.75}SbTe_2$	300	--	--	one singlet (or unresolved doublet) implies the presence of only one nickel site, Ni(1), while the other two Ni sites Ni(2) and Ni(3) remain unsubstituted	23S089
$Ca^{121}SnO_3$	Sb_2Te_3 and $(GeTe)_x(Sb_2Te_3)$ films: c-$Ge_3Sb_2Te_6$, c-$Ge_2Sb_2Te_5$, c-$GeSb_2Te_4$, a-$GeSb_4Te_7$	80	--	--	isomer shift δ ~ 5.1–5.5 mm/s is typical for the spectra of Sb^{3+} compounds; the structure environment is close to the local structure of the antimony atoms in Sb_2Te_3	23M058
Sn-119 23.80 keV Transition: Glasses and Amorphous Substances						
$Ca^{119mm}SnO_3$	Ge(Sn), SnTe, and amorphous $(GeTe)_x(Sb_2Te_3)$ films: a-$Ge_{2.95}Sn_{0.05}Sb_2Te_6$, a-$Ge_{1.95}Sn_{0.05}Sb_2Te_5$, a-$Ge_{0.95}Sn_{0.05}Sb_2Te_4$, a-$Ge_{0.95}Sn_{0.05}Sb_4Te_7$ and a-$Ge_{1.45}Sn_{0.05}Te_{8.5}$	80	--	--	Sn(IV) isovalently replace the four-valent germanium atoms, which form a tetrahedral chemical bond with atoms in their local surroundings	23M058
xx	$Li_xSi_{1-y}Sn_y$	300	--	--	previous observation that QS reaches a maximum value around 1.2 mm/s at $x \sim 1$ and decreases for lower and higher concentrations was explained with Eq. QS= a min {CLi,CSi} + b	23F017
Sn-119 23.80 keV Transition: Metals and Alloys						
xx	$Li_xSi_{1-y}Sn_y$	300	--	--	previous observation that QS reaches a maximum value around 1.2 mm/s at $x \sim 1$ and decreases for lower and higher concentrations was explained with Eq. QS= a min {CLi,CSi} + b	23F017
Sn-119 23.80 keV Transition: Miscellaneous Experiments						
$Ca^{119mm}SnO_3$	Ge(Sn), SnTe, and amorphous $(GeTe)_x(Sb_2Te_3)$ films: a-$Ge_{2.95}Sn_{0.05}Sb_2Te_6$, a-$Ge_{1.95}Sn_{0.05}Sb_2Te_5$, a-$Ge_{0.95}Sn_{0.05}Sb_2Te_4$, a-$Ge_{0.95}Sn_{0.05}Sb_4Te_7$ and a-$Ge_{1.45}Sn_{0.05}Te_{8.5}$	80	--	--	Sn(IV) isovalently replace the four-valent germanium atoms, which form a tetrahedral chemical bond with atoms in their local surroundings	23M058
$Ca^{119m}SnO_3$	$Ni_{3-x}Sn_xTe_2$ (x=0 to 1)	300	--	--	identified two non-equivalent sites (D1 and D2), characterized by low symmetry of the local environment and proposed the possible versions of tin environment	23S089
Sn-119 23.80 keV Transition: Miscellaneous Inorganic Compounds						
$Ca^{119mm}SnO_3$	Ge(Sn), SnTe, and amorphous $(GeTe)_x(Sb_2Te_3)$ films: a-$Ge_{2.95}Sn_{0.05}Sb_2Te_6$, a-$Ge_{1.95}Sn_{0.05}Sb_2Te_5$, a-$Ge_{0.95}Sn_{0.05}Sb_2Te_4$, a-$Ge_{0.95}Sn_{0.05}Sb_4Te_7$ and a-$Ge_{1.45}Sn_{0.05}Te_{8.5}$	80	--	--	Sn(IV) isovalently replace the four-valent germanium atoms, which form a tetrahedral chemical bond with atoms in their local surroundings	23M058
$Ca^{119m}SnO_3$	$Ni_{3-x}Sn_xTe_2$ (x=0 to 1)	300	--	--	identified two non-equivalent sites (D1 and D2), characterized by low symmetry of the local environment and proposed the possible versions of tin environment	23S089
Te-125 35.50 keV Transition						
Mg_3TeO_6	GeTe and and Sb_2Te_3 and crystalline and amorphous $(GeTe)_x(Sb_2Te_3)$ films	80	--	--	concluded that the local structures of tellurium atoms correspond to the structural units of GeTe and Sb_2Te_3 compounds	23M058

ABBREVIATION LISTING

--	multiple components
IS/	isomer shift relative to
v	variable
xx	material not reported

ISOTOPE INDEX

MÖSSBAUER MINERAL HANDBOOK

√ **Updated in 2005** Many sections completely updated through October 2005
√ **Reference Listing** All articles on minerals published in the ***Mössbauer Effect Reference and Data Journal***
√ **Review Reference Listing** Over 160 review articles related to minerals
√ **Special Reference Listing** Specialized bibliographical listings on several topics of interest, including: clays, coals, lavas, Mars, moon samples, meteorites, nodules, and soils
√ **Mineral Index** Over 400 minerals studied by Mössbauer spectroscopy
√ **Data Index** Mineral name, chemical formulae (when given), Mössbauer parameters of isomer shift, quadrupole splitting, and magnetic hyperfine interactions (includes uncertainty)
√ **Author Index** Names and current addresses for all authors of the publications in the *Reference Listing*

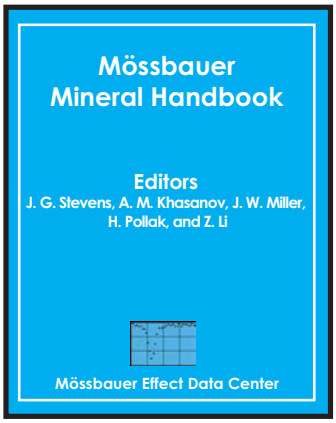

Soft-Cover Handbook or PDF Format on CD-ROM $ 290.00 US
For air mail postage and handling add 10% of total order

MÖSSBAUER HANDBOOKS

The **Mössbauer Handbooks** cover over twenty specialty areas of Mössbauer spectroscopy. Each handbook provides concise, ready access to all reference and data listings collected by the Mössbauer Effect Data Center on a specific topic (exceptions to the contents are noted in the listing of available handbooks).

√ **Reference Listing** All references on the specialty
√ **Subject Index** Topical index to the articles
√ **Author Index** Index of all authors
√ **Data Listing** Sources, absorbers, isomer shifts, quadrupole splittings, and other information (not included in all handbooks)

# Handbooks	Unit Price*
1	$70
5	$65
10	$60
20	$55
30+	$50

**Add 10% of total for Air Mail Shipping.*

Data at your fingertips...

Amorphous Materials (Two Parts by Content)
Biological Substances
Catalysis
Corrosion Studies
High Temperature Superconductors
Irradiation Experiment
Magnetic Hyperfine Distributions
Main Group Mössbauer Isotopes
(not ^{197}Au, ^{119}Sn or ^{121}Sb)
Microcrystals
Mössbauer Temperatures
(including Debye and Einstein)
Rare Earth Mössbauer Isotopes
(Two Parts by Content)
Relaxation
Reviews (Two Parts by Date)
Semiconductors (Two Parts by Content)
Surface Studies
Thin Films
Transition Metal Mössbauer Isotopes
(except ^{57}Fe and ^{197}Au)
^{197}Au Mössbauer Spectroscopy
^{121}Sb Mössbauer Spectroscopy
^{119}Sn Mössbauer Spectroscopy
(Five Parts by Date)

For more information, please visit MEDC's Web site <**www.medc.dicp.ac.cn**> or e-mail <**medc@dicp.ac.cn**>

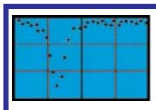

Mössbauer Effect Data Center

Dalian Institute of Chemical Physics
Chinese Academy of Sciences
457 Zhongshan Road, Dalian 116023, China
Phone: +86-411-84379159
Fax: +86-411-84685940
Email: medc@dicp.ac.cn

MÖSSBAUER SPECTROSCOPY
NEWSLETTER

March 2024

Design of Novel Fe(II) Colorimetric Sensors for Detection of Volatile Organic Compounds

Li Sun, Yann Garcia (✉)
Institute of Condensed Matter and Nanosciences, Molecular Chemistry, Materials and Catalysis (IMCN/MOST), Université catholique de Louvain, Place Louis Pasteur 1, 1348 Louvain-la-Neuve, Belgium
Email: yann.garcia@uclouvain.be

Bibliography

Dr. Li Sun

Dr. Li Sun was born in Shandong, China in 1991. She received her B.S. degree from Zaozhuang University in 2015. Then she pursued her M. Sc. degree in the group of Prof. Aiguo Wu and Prof. Haining Liu at the University of Chinese Academy of Sciences from 2015-2018. In September 2018, she entered the Inorganic-chemistry Ph.D. program at the UCLouvain, Belgium, where she subsequently joined the laboratory of Professor Yann Garcia, where she was trained to advanced Mössbauer spectroscopy of spin crossover materials. Her research is focused on using and developing Fe(II) sensors to distinguish VOCs and assessment the freshness in high-protein food.

Prof. Dr. Yann Garcia

Prof. Dr. Yann Garcia was born in Castres, France in 1972. He obtained his doctorate in material science and solid state chemistry from the Univ. of Bordeaux at the ICMCB-CNRS under the supervision of Prof. O. Kahn in Jan. 1999. He then joined the Institute of Inorganic and Analytical Chemistry of the Univ. of Mainz (Germany) to work with Prof. Dr. Philipp Gütlich as a TMR EU post-doctoral fellow. While getting a CNRS permanent position (Sorbonne Univ.), he was appointed assistant prof. at UCLouvain in 2001, associate Prof. in 2004, Prof. in 2009 and head of the Molecular Chemistry, materials and catalysis division of the IMCN institute in 2023. The research interests of Prof. Garcia extend from photoswitchable coordination compounds, spin crossover materials to smart sensors, medicinal and environmental applications, where Mössbauer spectroscopy is considered as a key tool. Prof. Garcia has published more than 290 publications with several cover pages of top chemistry journals and book chapters. Prof. Garcia is associate editor of the Mössbauer Effect Reference Data Journal (Chinese Academy of Sciences). He edited together with Prof. J. Wang and Prof. Zhang a book on Mössbauer spectroscopy focused on chemistry (Wiley VCH, 2024). He is president of the French Speaking Mössbauer Society (GFSM, www.gfsm.fr) and IBAME vice chair (www.ibame.org).

Introduction and context

Volatile organic compounds (VOCs), which can enter the human body through the respiratory tract, skin, and diet, can cause discomfort to the human body when certain limits are reached, leading to poisoning or even death in severe cases.[1-3] Therefore, to establish a healthy and safe living environment, detecting and analyzing VOCs are one of the hottest research directions in modern analytical chemistry. These analytes are widely distributed in biochemical, environmental and food samples. Despite their simple structure, they play an irreplaceable role and are linked to drug design and evaluation, clinical testing and treatment, environmental pollution, control and food safety regulation.[1] For example, the excess of VOCs in the living environment can enter the human circulatory system through the respiratory tract or food chain, inducing many diseases and even cancer[1]; and different kinds of VOCs and bacteria produced by food spoilage, misuse of which leads to the immune function of the human body declines. It will thus have a pathological impact on the human body that cannot be ignored. Therefore, establishing a rapid, effective, accurate, and reliable method for analyzing and detecting VOCs has essential theoretical and practical applications.

Relying on large equipment detection technology is costly; the sophisticated operation of precision instruments requires definitively professionals.[4-5] It is however not easy to achieve widespread popularity and convenient, rapid, real-time detection. At the same time, VOC analysis samples are usually accompanied by many interfering substances, which must be removed as much as possible before detection, and efficient sample pre-treatment technology is also a huge challenge for modern large-scale testing equipment. In recent years, sensing-based detection methods such as "electronic nose" and "electronic tongue" have provided new ideas for rapidly and conveniently detecting mixed analytes.[6] Unlike the traditional single-component analysis, this method considers complex mixed objects as a whole and completes the identification analysis through integrated sensing signal output, which is fast and efficient. Its disadvantage is that it requires complex post-data processing and pattern recognition techniques to obtain sufficient information. It is often unable to overcome the signal overlap of structurally similar components due to the lack of precise chemical recognition. The advent of colorimetric sensors has provided a solution to this problem.[7] By simulating the noses of humans and animals, information is obtained about the whole of the detected object, hence detection technology is expected to bring an essential breakthrough in the efficient, rapid and real-time detection of VOCs. In Li Sun's thesis,[8] the shortcomings of high cost, low sensitivity, and poor selectivity faced by VOCs identification, and identification VOCs were selected as the research object and an individualized colorimetric sensing detection chip was designed to improve the detection performance significantly. The thesis was defended in January 2023 at UCLouvain, Lavoisier building, IMCN institute in front of several international scientists including Prof. Yann Garcia (Vice-chair IBAME), Prof. Xavier Urbain (UCLouvain, Chair of the jury), Prof. Kamel Boukheddaden (Université Paris-Saclay, France), Prof. Wim Dehaen, (KU Leuven, Belgium), Prof. Michael Singleton (Secretary of the jury), Dr. Koen Robeyns (UCLouvain).[8] The main research work includes several aspects which are developed below:

1. A 3D Fe(II) metal-organic framework with SCO properties for colorimetric detection of $CHCl_3$

In order to design and prepare complexes at low cost, the synthesis steps need to be simple and afford considerable yields, pyridine ligands being the best candidates. Therefore, in this section, we report on the synthesis, crystal structures and magnetic behavior of a series of novel 3D MOF material built from 4,4' bipyridine like-ligands (**Scheme 1**) and $[N(CN)_2]^-$ (dca) organic bridges as well as 4,4' bipyridine ligands (bipy), $[Fe(bipy)_2dca]ClO_4$•Guest (**1**•Guest = **1**•$CHCl_3$•CH_3OH), and determined its guest-dependent spin crossover (SCO) behavior (host-guest interaction), accompanied with color and magnetic change by introducing $CHCl_3$ guest molecules in the cavities of the 3D framework (**Figure 1** and **2**).[9]

Interestingly, the complex **1**•$CHCl_3$•CH_3OH has turned out to exhibit a remarkable SCO transformation process, accompanied by a color change, involving the reversible exchange of small volatile molecules at room temperature (from orange to brown, 298 K) and low temperatures (from orange to dark brown, 77 K). Indeed, a SCO behavior with a thermal hysteresis loop of 15 K width ($T_{hy}^{\uparrow}$ = 195 K and $T_{hy}^{\downarrow}$=180 K) was identified. These transformations are coupled

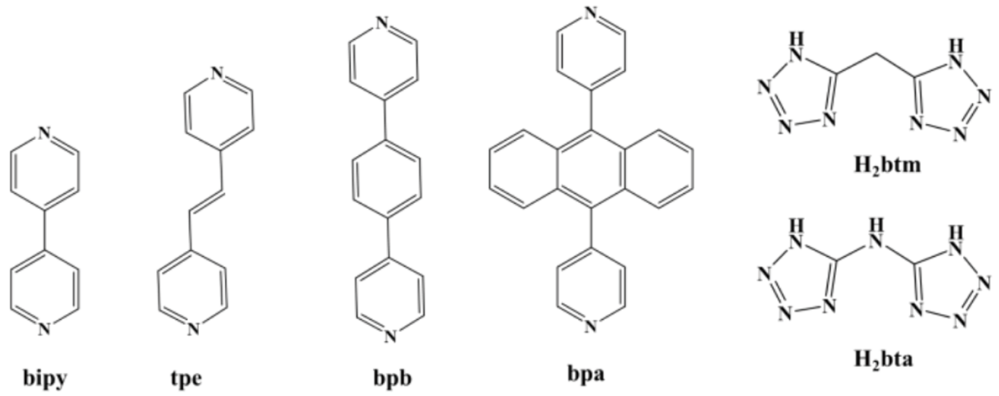

Scheme 1. The ligands used in Li Sun's thesis for synthesizing Fe(II) coordination compounds.

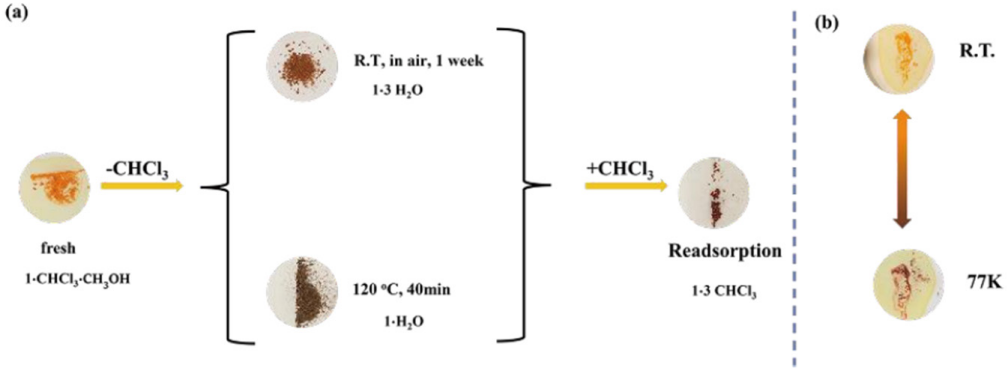

Figure 1. Color changes of (a) **1**•$CHCl_3$•CH_3OH, **1**•$3H_2O$ and **1**•H_2O and reabsorption (**1**•$3CHCl_3$) at room temperature (b) **1**•$CHCl_3$•CH_3OH at 77 K and room temperature.

to dramatic optical, magnetic, and crystallographic changes, thus converting this porous material into a robust switch, sensitive to $CHCl_3$ molecules, paving the way for the design of a new generation of sensors based on 3D SCO MOFs. Worth to notice that the hysteresis temperatures, T_{hy}, useful to accurately described hysteresis width in SCO materials, were for the first time here introduced in the literature.[9]

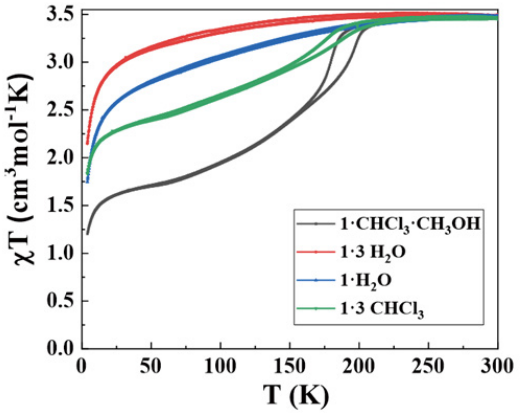

Figure 3. χT *vs.* T for **1**•$CHCl_3$•CH_3OH, **1**•$3H_2O$ (dried one week, at r. t.), **1**•H_2O (heated at 393 K for 40 min), and **1**•$3CHCl_3$ (after re-absorption of $CHCl_3$).

The 3D Metal-organic framework (MOF) colorimetric sensing chip (**1**•Guest) with a specific response to $CHCl_3$ was prepared by liquid-liquid phase diffusion. At room temperature, the colorimetric sensing chip displays orange and brown colors, accompanied by different magnetic properties at the lock and escapement of chloroform molecules. At low temperatures, with the induction of chloroform molecules, the colorimetric sensor changes from orange to dark brown, accompanied by a significant change in magnetic property, due to spin crossover.

2. Stimuli-responsive 3D MOFs SCO compounds showing a color change for $CHCl_3$/CH_2Cl_2

In section 1, we designed and prepared the Fe(II) SCO MOF colorimetric sensor, **1**•Guest, which has excellent potential to be developed as a sensor and memory device. However, on one hand, it was found that **1**•Guest only responds to chloroform molecules; on the other hand, the transition temperature of Fe(II) spin state in **1**•Guest is relatively low with the induction of chloroform molecules. Therefore, to further extend the specific response of such Fe(II) SCO

MOFs to different analytes, and at the same time, increase the spin state transition temperature, this section will continue to progress on the design and preparation of novel pyridine-based ligand inclusion compounds in conjunction with the previously discussed design concept of Fe(II) colorimetric SCO MOF sensors to investigate their specific response behavior to different analytes. In this part, we attempt to further replace the ligands by longer pyridine-like ligands with *trans*-1,2-bis(4-pyridyl)ethene (**tpe**), 1,4-bis(4-pyridyl)benzene (**bpb**), and 9,10-bis(4-pyridyl)anthracene (**bpa**) (**Scheme 1**), and successfully synthesize a new series of SCO 3D MOFs $[Fe(tpe)_2dca]ClO_4 \cdot 5CHCl_3 \cdot 3CH_3OH$ (**2**•$5CHCl_3$•$3CH_3OH$), $[Fe(bpb)_2dca]ClO_4 \cdot 3CHCl_3 \cdot 0.5CH_3O$-H(**3**•$3CHCl_3$•$0.5CH_3OH$), and $[Fe(bpb)_2dca]ClO_4 \cdot 2.5CH_2Cl_2 \cdot 0.5CH_3OH$ (**3**•$2.5CH_2Cl_2$•0.5C-H_3OH).[10] And a novel 3D MOF, $[Fe(bpa)_2(SCN)_2]$•solvent, lacking SCO behavior.[11] Interestingly, the study shows that the release of interstitial $CHCl_3$ molecules from a crystal of (**2**•$5CHCl_3$•$3CH_3OH$), which was dried at room temperature for one day was accompanied by a change in magnetic properties as well as a color from red to dark brown (**2**•$CHCl_3$•$2H_2O$) (**Figure 3**). In addition, **3**•$3CHCl_3$•$0.5CH_3OH$ and **3**•$2.5CH_2Cl_2$•$0.5CH_3OH$ crystals show different colors (yellow and orange, respectively) due to differences in solvent molecules ($CHCl_3$ and CH_2Cl_2, respectively) in their crystal lattice (**Figure 3**). The different SCO properties of these three crystals were verified by magnetic measurements, where the transition temperatures of the SCO were significantly shifted by the solvent change (**Figures 4** and **5**). These MOFs can therefore be used as detectors for monitoring $CHCl_3$ and CH_2Cl_2 and potentially other VOCs that can be accommodated in these structures.

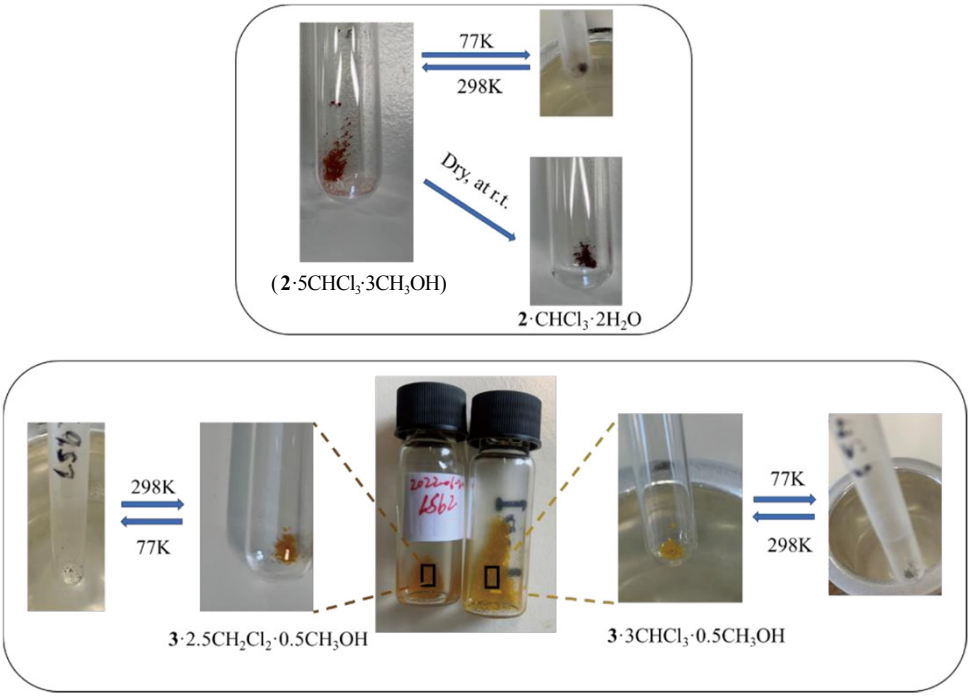

Figure 3. Color changes of (a) **2**•$5CHCl_3$•$3CH_3OH$ (b) **3**•$3CHCl_3$•$0.5CH_3OH$ and **3**•$2.5CH_2Cl_2$•$0.5CH_3OH$.

The temperature dependence of the χT product was generated (where χ is the molar magnetic susceptibility and T is the temperature) for different phases of compounds **2**•Guest by cooling and heating, to study the guest effect on the SCO properties in **Figure 4**. The spin state of magnetic centers in **2**•$5CHCl_3$•$3CH_3OH$ were further confirmed by variable-temperature magnetic susceptibility measurements ($T_{1/2}$ ~ 155 K). As shown in **Figure 4a**, crystalline **2**•$5CHCl_3$•$3CH_3OH$ undergoes an incomplete spin transition in the range of 4 K to 300 K. In the cooling process, **2**•$5CHCl_3$•CH_3OH retains the HS state to 226 K and then gradually decreases and reaches a plateau with a χT value of 2.00 cm^3 mol^{-1} K at 63 K. No thermal hysteresis was detected in the SCO transition, even considering the heating process. The second run of magnetic data decreases more slowly than the first run and is more gradual and incomplete, possibly after partial escape of solvent molecules, reducing the interaction between guest•••guest and

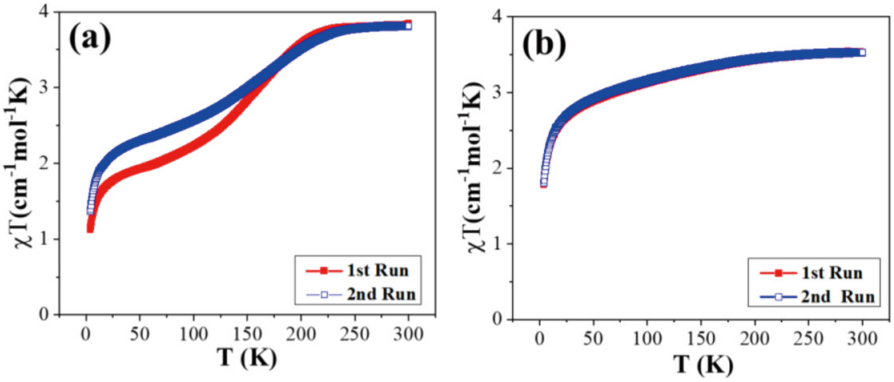

Figure 4. χT *vs.* T for (a) **2**•5$CHCl_3$•3CH_3OH and (b) **2**•$CHCl_3$•2H_2O.

host•••guest molecules. This result is confirmed by the magnetic data of sample **2**•$CHCl_3$•2H_2O, which shows that the Fe(II) ion centers, show almost exclusively a HS state in the range of 4 K to 300 K (**Figure 4b**).

The temperature dependence of χT was also produced for different phases of compounds **3**•Guest by cooling and heating, to study the guest molecules effect on the SCO properties (**Figure 5**). For all compounds, the χT values are around 3.8 cm^3 mol^{-1} K at room temperature, indicating that all Fe(II) centers are in the HS state (S = 2). **3**•3$CHCl_3$•0.5CH_3OH and **3**•2.5CH_2Cl_2•0.5CH_3OH exhibit a gradual and incomplete SCO behavior. For **3**•3$CHCl_3$ •0.5CH_3OH, $T_{1/2}$ ~ 85 K as the temperature decreases, and there is no hysteresis (**Figure 5a**). When the temperature is reduced to 45 K, the HS distribution of 87% is still maintained. However, for **3**•2.5CH_2Cl_2•0.5CH_3OH, an incomplete two-step SCO behavior is observed, accompanied by a very narrow hysteresis loops, involving ~7% of FeII ions in the first step, from 250 K to 180 K with $T_{1/2}^{\uparrow}$ ~ 219 K and $T_{1/2}^{\downarrow}$ ~ 217 K, and ~41% of FeII ions, from 180 to 33 K, with $T_{1/2}^{\uparrow}$ ~ 125 K and $T_{1/2}^{\downarrow}$~ 122 K). Thus, magnetic properties data indicate that solvent molecules ($CHCl_3$ or CH_2Cl_2) can induce different SCO behaviors. In addition, the clathrate with CH_2Cl_2 ($CHCl_3$) molecules show a color change from orange (yellow) to almost black (dark brown), on cooling from 298 K to 77 K. When solvent molecules escape from the crystal lattice on warming at 120 °C for 40 min, the SCO behaviors of the resulting compounds (**3**•1.5$CHCl_3$•2H_2O and 3•CH_2Cl_2•2H_2O) are cancelled (**Figure 5b**). Indeed, central FeII ions are almost no longer sensitive to temperature change and show a HS state over the whole temperature range. To further study the effect of solvent molecules on the SCO behavior of complexes, we shall take **3**•2.5CH_2Cl_2•0.5CH_3OH as a representative example (**Figure 5c**). First of all, the magnetic properties of this material were recorded on cooling, from 300 K to 4 K, and then on warming back to 300 K, as a first run, showing the expected two-step SCO behavior observed on **Figure 5a**. After that, the sample was cooled to 4 K, and warmed up again, this time to 400 K, and maintained at this temperature for 30 min, as the second run. The χT values are similar in the first two cycles from 4 K to 300 K, although a small deviation is observed below 150 K. After annealing at 400 K, the χT profile for the third run on cooling and warming back to 400 K, shows a paramagnetic like behavior involving a few spins. Nevertheless, the χT values are maintained to 3.5~3.8 cm^3 mol^{-1} K, whatever the run, which indicates that almost all Fe(II) ions remain in the HS state after solvent molecules are partially removed from the cavities of the compound. Therefore, the behavior of the vanishing SCO behavior might be attributed to the deterioration of host-guest interactions and deformation of the framework during desolvation. From the study of magnetic data, it is found that SCO MOF **3** has a special response not only to $CHCl_3$ but also to CH_2Cl_2. Therefore, compared with the material in the previous part (**1**•$CHCl_3$•CH_3OH), SCO MOF **3** has an expanded response range.

In section 2, to expand the detection range of colorimetric sensing chips for VOCs and to increase the conversion temperature of SCO complexes, new 3D MOF SCO colorimetric sensing chips (**2**•Guest and **3**•Guest) were prepared due to changing the length and functional groups of the ligands. It was shown that **2**•Guest (red, 298 K; almost black, 77 K) could only correspond precisely to chloroform, with the presence or absence of chloroform molecules, which have different colors, red to brown. But, with further changes in ligand molecules, it was found that chloroform and dichloromethane in

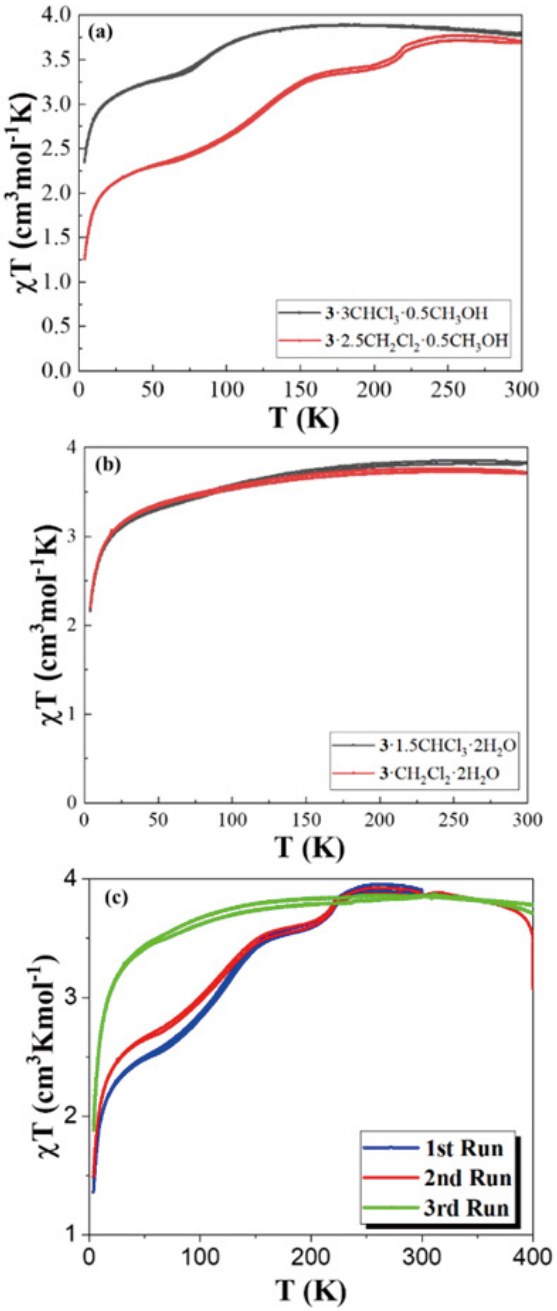

Figure 5. (a) and (b) χT *vs.* T for **3**•Guest molecules, (c) χT *vs.* T for **3**•2.5CH_2Cl_2•0.5CH_3OH.

the crystal lattice can induce the color change of **3**•Guest effectively and precisely. At room temperature, the crystal of **3**•Guest presented yellow or orange, and the central Fe(II) ions will remain in the HS state; at low temperature, the crystal will appear dark brown or almost black, and the central Fe(II) irons will stay in the LS state.

3. A colorimetric sensor for the highly selective and rapid detection of VOCs and hazardous gases

It was learned in section 2 that complex **3**•Guest is capable of responding to $CHCl_3$ and CH_2Cl_2, but its detection range has not been extended to a great extent. To design a colorimetric sensor for the detection of a wide range of analytes at room temperature, complex **4** was designed and prepared.[12] This complex not only has a broad selectivity for VOCs, accompanied by a significant color change for naked-eye observation but also has a relatively short response time. Therefore, this material has excellent value for potential applications in environmental monitoring.

To aim, our group reported on a mononuclear Fe(II) neutral complex chemically responsive pigment with the ability to differentiate four different TICs and methanol/ethanol among other alcohols.[13-14] This system is now modified to a unique colorimetric sensor with the formula $[Fe(H_2btm)_2(H_2O)_2]Cl_2$ (**4**) (H_2btm = di(1H-tetrazol-5-yl)methane), allowing to detect at real-time, with high selectivity, VOCs and HGs under ambient conditions by the naked eye, which is groundbreaking. In particular, it rapidly detects and discriminates vapors of $NH_{3(g)}$ and amines in the gas phase by showing different colors (**Figure 6**). The study of the mechanism revealed a conformation spin state switching after adsorption. Furthermore, a friendly smartphone-based analytical method was developed to make **4** accessible for in-field applications. Most interestingly, an obvious color change was observed upon guest contact and recorded by outputting RGB1 (red, green, and blue) and HSB2 (hue, saturation, and brightness) values directly. The recorded data were then analyzed by a simple and intuitive standard chemometric means (HCA) (**Figure 7**). Forasmuch, it indicates that **4** has broad application prospects in environmental protection and food safety assessment, as an in-field naked-eye colorimetric sensor.

Selectivity of the VOCs colorimetric sensor. As observed by the naked eye, **4** can detect and distinguish a wide range of hazardous VOCs at room temperature (**Figure 6**). In order to undertake a simple and effective comparison by recording the color change of **4** for each guest analyte, we have used an application to convert sensor pictures printed on smartphones into digital information. Therefore, there was no need to keep the discolored images. We have used the most simple and effective statistical method to record and analyze collected data, called HCA, which is a classification scheme based on the Ed

Figure 6. Images depicting vapochromic transformation on the sensing of VOCs by complex **4** for 120 min, at room temperature, on ground crystals.

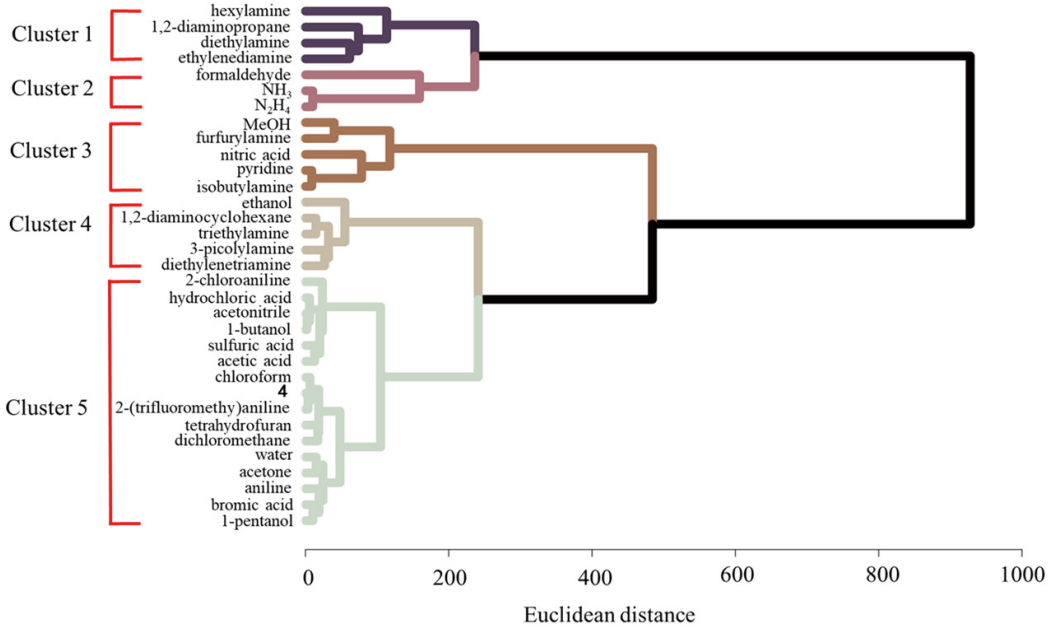

Figure 7. HCA for 32 VOCs at saturation concentrations and a control.

(the Euclidean distance between two points in Euclidean space is the length of a line segment between the two points) of data points in their full dimensions.[15] It uses, in addition, minimum variance for clustering (which is known as the "Ward's method").[16] Each experiment is defined as 6-dimensional vectors, which are composed of six RGB1 (red, green, and blue) and HSB2 values (hue, saturation, and brightness). These data are used to quantitatively compare the color changes of images from **Figure 6**.[14, 17-18] Then, we are simply comparing the spatial distance by the HCA between the observed colors "before" and "after" VOCs contact, the color-change profiles being inherently digital data, which can therefore be easily handled by routine chemometric analysis.[19] HCA is based on the Ed between these vectors in this six-dimensional RGB1 and HSB2 value space, thereby generating a dendrogram, as shown in **Figure 7**. There are five groups of 33 samples, which imply five kinds of colors after adsorption.

^{57}Fe Mössbauer spectroscopy analysis of 4 towards different vapors. ^{57}Fe Mössbauer spectra of **4**, at 298 K, show one quadrupole doublet with an isomer shift δ = 1.15(1) mm. s^{-1} and a quadrupole splitting ΔE_Q = 3.66(1) mm. s^{-1} of area fraction A = 100%, where the parameters are typical for HS Fe(II) ions (Figure 8a).[20-21] After adsorbing $NH_{3(g)}$ molecules, for **4**@NH_3 (**Figure 8b**), a new quadrupole doublet emerges in the center [δ = 0.38(1) mm. s^{-1}; ΔE_Q = 0.23(1) mm. s^{-1}] of area fraction A = 70%. These parameters are characteristic of LS Fe(II) ions in a FeN_6 core. Indeed, the replacement of the oxygen atoms with nitrogen atoms, which are less electronegative, increases the electronic

density of s electrons in the vicinity of the iron nucleus and thereby decreases the isomer shift. [22] The remaining contribution corresponds to the HS Fe(II) site: HS [δ = 1.08(1) mm. s^{-1} ; ΔE_Q = 3.51(3) mm. s^{-1}; and area fraction A = 30%]. Not all Fe sites are switched, which could be due to crystallographic modifications that restrict further $NH_{3(g)}$ molecules diffusion. For **4**@N_2H_4 (**Figure 8f**) and **4**@isobutylamine (**Figure 8e**), it shows new quadrupole doublet with δ = 0.39(3) mm. s^{-1} and δ = 0.38(1) mm. s^{-1}, with ΔE_Q = 0.20(5) and 0.08(3) mm. s^{-1}, respectively. These parameters are typical for LS Fe (II) ions, indicating that **4** absorbs $N_2H_{4(g)}$ and isobutylamine(g) molecules to form a part of the LS FeN_6 center. This indicates that the invasion of gas-phase VOCs molecules causes a redistribution of 3d orbital electrons of Fe(II), leading to a part of HS states being converted to the LS states. Furthermore, the radius of N atoms is smaller than that of O atoms, and the electronegativity is also smaller. So, it is easy to form a strong coordination field between N and Fe(II) ions. There is no doubt that N atoms of VOCs molecules replace O atoms and coordinate with the central iron atom (on the surface of the crystals) after **4** is exposed to VOCs gas-phase molecules, thereby constructing an LS FeN_6 core together with the azole ligands from HS FeN_4O_2.

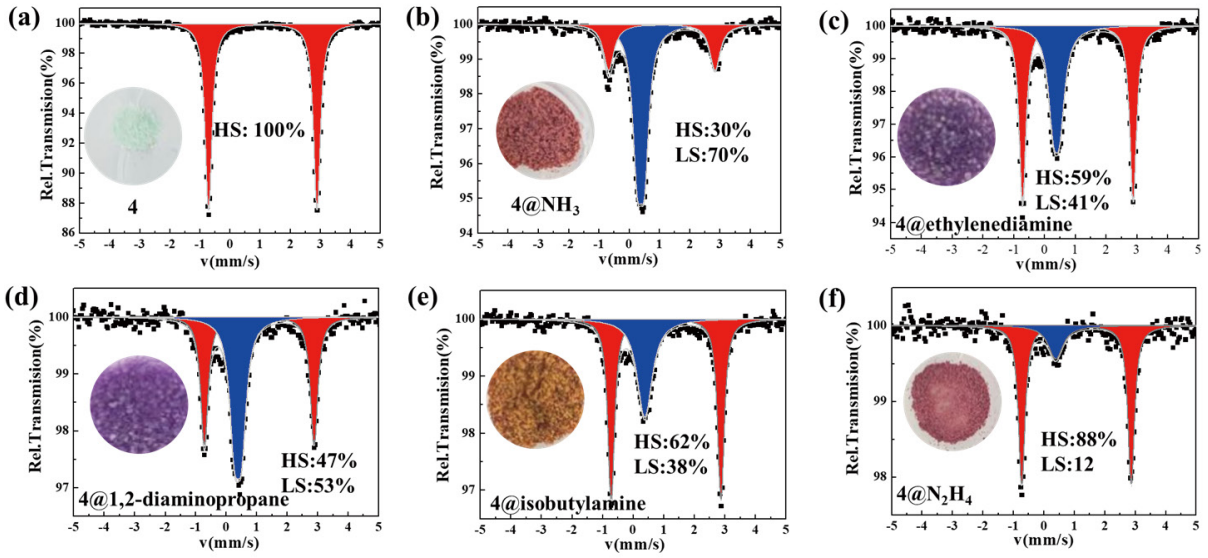

Figure 8. Spin state population at room temperature by ^{57}Fe Mössbauer spectroscopy of **4** before and after adsorption of different guest molecules at room temperature.

Magnetic properties analysis of 4 towards different vapors. The changes in the spin state observed for the various transformations described above provide this material with potential as a spin-based chemosensor. This is further investigated by variable-temperature magnetic susceptibility measurements on polycrystalline samples after VOCs gas-phase adsorption over the range of 4−400 K under a constant field of 1 T. From **Figure 9**, SQUID magnetometry demonstrates lower χT values for samples after VOCs adsorption compared to **4** at 298 K, which show a full paramagnetic state with χT = 3.60 cm^3 mol^{-1} K, corresponding to Fe(II) ions (S = 2, HS state), which is consistent with the observations from single-crystal X-ray diffraction. For instance, **4**@NH_3 showed a dramatic modification of its spin state since it is mostly diamagnetic at 300 K with χT = 0.50 cm^3 mol^{-1} K, in agreement with ^{57}Fe Mössbauer data. Upon heating from 298 to 400 K, χT was found to increase, presumably due to solvent release, which involves a change in spin state, although not all. The observations directly prove that a spin state switching process accompanies the adsorption or desorption of ammonia and VOCs guest-phase molecules of **4**. Foremost, magnetic properties of after adsorption of other VOCs are consistent with ^{57}Fe Mössbauer spectroscopy data.

In this section, to improve the detection range of colorimetric sensors and further quantify the content of VOCs, a new colorimetric sensor of formula $[Fe(H_2btm)_2(H_2O)_2]Cl_2$ (**4**) (H_2btm = di(1H-tetrazol-5-yl)methane) was produced, allowing for detection in real-time, with high selectivity and sensitivity, 14 different hazardous gases. In particular, amines are detected very quickly with high sensitivity. The detection

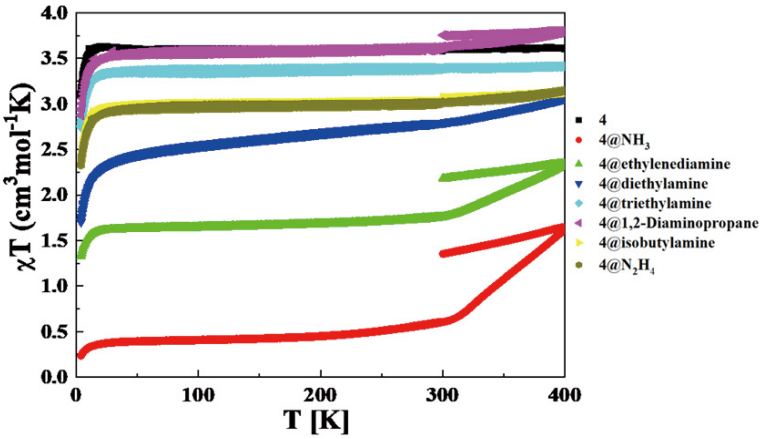

Figure 9. Temperature-dependent χT plots for **4** before (black) and after adsorption of different guest molecules.

is accompanied by significant and fast color changes detectable by the naked eye under ambient conditions. In addition, different VOCs could be distinguished by simple and intuitive standard chemometric means using a handful of smartphone-based methodical methods, offering a large color panel depending on detected molecules. The crystal lattice of **4** reconstructs after adsorbing VOCs vapors, which is accompanied by a spin state and a color change. This sensor is low-cost, easy to use, and delivers excellent and fast detection. Such features offer attractive prospects for **4**, which could be used for in-field detection and food safety control in environmental conditions.

4. A non-porous Fe(II) complex for the colorimetric detection of hazardous gases and the monitoring of meat freshness

In recent years, with the continuous improvement of the quality of life, the demand for safe food and a healthier environment has been increasing, thus making food quality monitoring and assessment, a constant concern.[23-25] In this section, we propose a simple strategy to fabricate a Fe(II) based colorimetric platform ($[Fe(Hbta)_2(H_2O)_2]\cdot 2H_2O$ (**5**) with H_2bta = bis(1Htetrazol-5-yl)amine)[26]. It undergoes a color change when treated with some harmful vapor molecules (listed in **Figure 10**), especially, ammonia and some amines vapors. This complex was used for NH_3 quantitative detection, in the frame of the visual real-time and in-situ monitoring of meat spoilage by a simple color recognizing smartphone software. Our findings open up new prospects for exploring various Fe(II) based materials for sensing hazardous and noxious substances, and show tremendous promise in applications for food status monitoring and environmental quality assessment.

^{57}Fe Mössbauer spectroscopy analysis. The spin state of **5** after hazardous gases absorption was confirmed by ^{57}Fe Mössbauer spectroscopy measurements carried out at room temperature in transmission mode (**Figure 11**). At room temperature, the spectrum of **5** shows a quadrupole doublet which was fitted by Lorentzian lines to yield isomer shift δ = 1.10(2) mm.s^{-1} and quadrupole splitting ΔE_Q = 3.78(3) mm.s^{-1}. Such parameters are typical for octahedral Fe(II) ions in the HS state (**Figure 11a**).[12] This result agrees well with the magnetic susceptibility measurement which shows 100% of HS Fe(II) ions at room temperature. LS Fe(II) ions were detected as a result of a partial spin state change from HS to LS after adsorbing hazardous gases with amines. For instance, **5**@NH_3 displays four quadrupole doublets assigned to two HS Fe(II) ions (HS1 Fe(II) and HS2 Fe(II)) (area fraction = 14 and 10%; δ = 0.89(2) and 1.18(9) mm.s^{-1}; ΔE_Q = 3.42(5) and 2.00(2) mm.s^{-1}, respectively, red and pink spectra) and a LS Fe(II) (area fraction = 41%; δ = 0.25(2) mm.s^{-1}; ΔE_Q = 0.78(8) mm.s^{-1} at room temperature, light blue spectra), as well as a LS Fe(III) (area fraction = 35%; δ = 0.20(2) mm.s^{-1}; ΔE_Q = 1.49(6) mm.s^{-1} at room temperature, navy blue spectra) (in **Figure 11b**). These parameters (light blue spectra) are characteristic of LS Fe(II) ions in a FeN_6 core, due to O atoms replacement by N atoms to coordinate with Fe(II) after amines (ammonia) adsorption.[14] Other analogue displays similar LS Fe(II) spectra in **Figure 11**. After adsorbing the gas-phase molecules with amino groups, which may form different interactions with the central atom and surface molecules, a new spin state is generated. Such a result is confirmed by magnetic measurements, and shows the remarkable input of ^{57}Fe Mössbauer spectroscopy in this analysis.

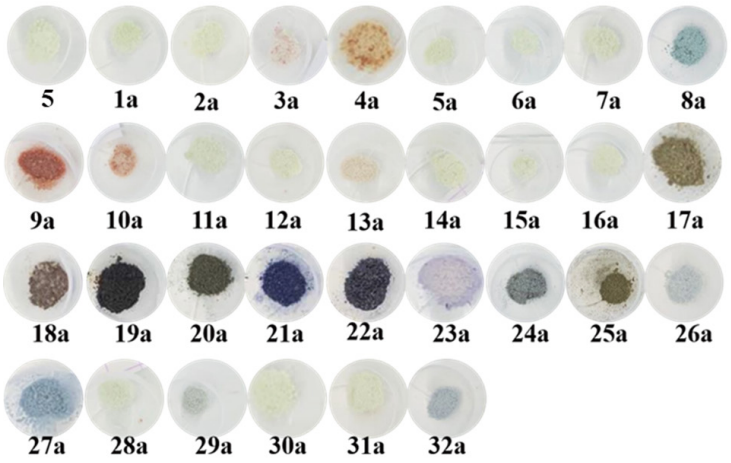

Figure 10. Colorimetric sensor (**5**) responses for 32 common analytes atsaturation vapor pressure at room temperature.(**1a** = H_2O; **2a** = acetonitrile; **3a** = formaldehyde; **4a** = dichloromethane; **5a** = chloroform; **6a** = acetone; **7a** = tetrahydrofuran; **8a** = pyridine; **9a** = MeOH; **10a** = ethanol; **11a** = 1-butanol; **12a** = 1-pentanol; **13a** = hydrochloric acid; **14a** = hydrogen bromide; **15a** = acetic acid; **16a** = sulfuric acid; **17a** = nitric acid; **18a** = NH_3; **19a** = isobutylamine; **20a** = diethylamine; **21a** = 1,2-diaminopropane; **22a** = ethylenediamine; **23a** = N_2H_4; **24a** = diethylenetriamine; **25a** = furfurylamine; **26a** = hexylamine; **27a** = triethylamine; **28a** = aniline; **29a** = 3-picolylamine; **30a** = 2-(trifluoromethyl)aniline; **31a** = 2-chloroaniline; **32a** = 1,2-diaminocyclohexane.)

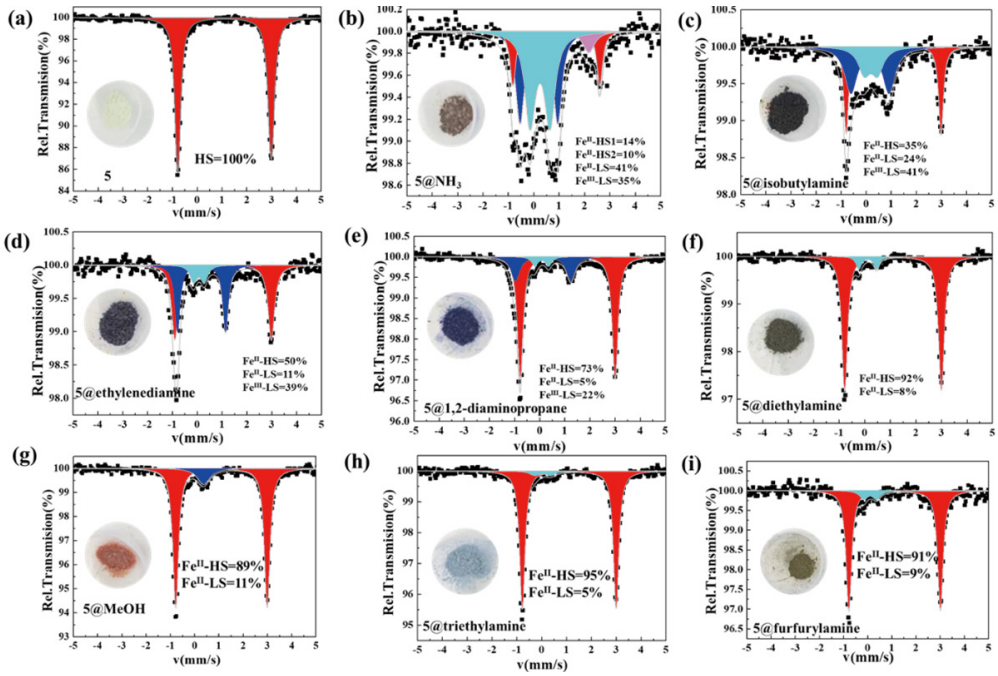

Figure 11. Spin state population at room temperature by ^{57}Fe Mössbauer spectroscopy of **4** before and after adsorption of different guest molecules at room temperature.

5. Applications in the assessment of meat freshness.[26]

Ammonia has been used as an important indicator of food spoilage state. In order to verify the practical application property of our colorimetric sensor detection system, it was used to real-time and in-situ detect $NH_{3(g)}$ from real meat samples and to evaluate meat freshness at room temperature (23±1 ^{o}C). Euclidean distance-based in-situ monitoring of meat samples was then performed over time (**Figure 12a**). The distance was shown to increase quickly after 24 h, especially for chicken meat, which indicates that the chicken spoilage rate is relatively fast, and the release of ammonia gas is relatively high too. The accurate concentration of ammonia vapor in the sample was measured using an electronic ammonia gas detector (AR8500) as standard control (**Figure 12b**). No ammonia release was observed before 24 h at room temperature (23+1

°C) for the meat of chicken (breast), pork (belly), and beef (steak) packs. However, the situation differs after 36 h with 3.6 ppm (for chicken), 0.2 ppm (for pork), and 0.2 ppm (for beef) levels. At 48 h, 24.7 ppm were detected for chicken, 1.2 ppm for pork, and 0.9 ppm for beef. (This result is consistent with the experimental result of 5 in **Figure 12a**). To better reveal the complex system's capabilities to quantitatively assess meat freshness, HCA analyses were conducted on the database collected for spoilage of meat samples. HCA manifests the clustering of data with three distinct classes of responses, which means there are three processes of meat from fresh to spoilage, as shown in **Figure 12c**. The cluster with the lowest response is the freshest meat, which was labeled "Fresher", which contains 0 h storage of three meats (as control), and from 12 h to 24 h storage of chicken, beef, and pork (The result is consistent with **Figure 12a** and **12b**, which shows no ammonia gas release from meats from 0 h to 24 h). The middle response cluster, labeled "less fresh", contains 36 h storage of pork and beef meat as well as 48 h storage of beef (Ammonia release has been detected, but not much from 24 h to 48 h for pork and beef meat, in **Figure 12a** and **12b**). The most responsive cluster, labeled "spoiled", includes the 36 h storage of chicken, 48 h storage of chicken and pork, and 60 h storage of chicken, pork, and beef meats (The release of ammonia is too high, but after 48 h, the release of ammonia is relatively fast, in **Figure 12a** and **12b**).

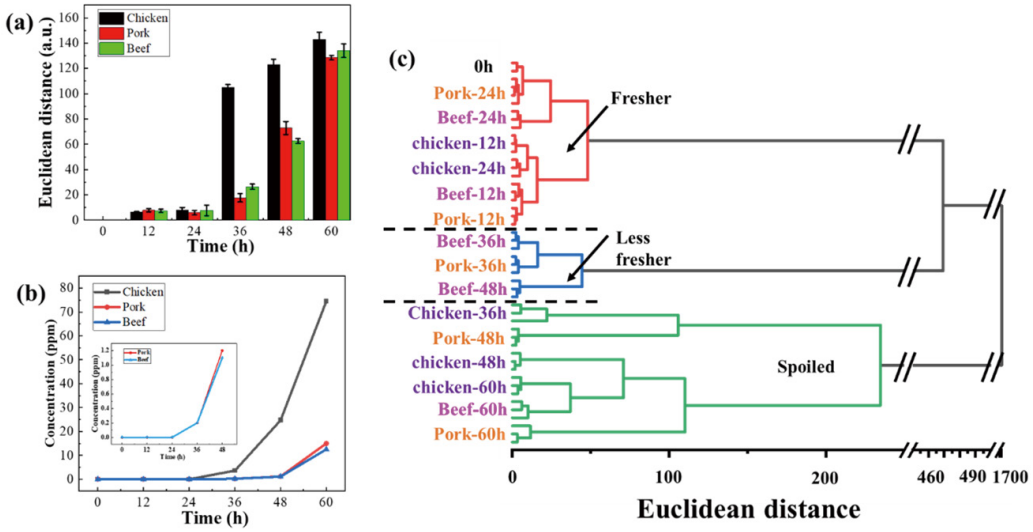

Figure 12. (a) Response of **5** to three meat products stored at room temperature (23±1 °C), (b) concentrations of ammonia were measured by ammonia gas detector from meat products at room temperature (23±1 °C) (insert: Response of **5** to low concentration of ammonia), (c) dendrogram showing hierarchical cluster analysis of the spoilage of meat (chicken, beef and pork) at room temperature (23±1 °C) with different time.

Conclusion

In short, colorimetric sensors (**4** and **5**) with excellent responses to various harmful gases were prepared by coordinating bis-tetrazole ligands (H_2btm and H_2bta) with Fe(II) ions, respectively, and their response to analytes was speedy. In addition, after colorimetric sensors **4** and **5** were exposed to the harmful gas, the color changes obviously, and the naked eyes can distinguish the color change at room temperature. However, everyone's perception of color is inconsistent, so it is not easy to obtain objective research results. Therefore, picture information was converted into digital information through a smartphone. Then the digital information was analyzed in combination with the corresponding digital analysis method (HCA) to establish the most suitable analysis model for the research system. Finally, positive progress was also made in the application of colorimetric sensors for real sample analysis. In an experiment, the colorimetric sensor **5** and meat food (meat of chicken, pork, or beef purchased in a downtown supermarket) were joined together in one bottle at room temperature. With the increase of time, different colors of colorimetric sensors (the ammonia gas released by meat spoilage caused the sensor to change color) were obtained. Then, the freshness of the meat was assessed by comparing the difference in the sensor's color. The results showed that the colorimetric sensor **5** indeed has excellent potential practical application value. Therefore,

the smartphone-based colorimetric sensor system can detect harmful gas analytes in a wide range and has high sensitivity. Its operation is simple and fast, and it can also detect analytes in situ and in real-time. This colorimetric sensor system has also achieved positive results in meat freshness assessment studies (**Figure 13**).

Therefore, our study offers a fundamental guarantee for food security in underdeveloped areas.[27] An appealing perspective focus on a multidisciplinary research and communication network in response to the detection of gases released during food spoilage, involving the entire value chain from food preservation to consumer products. In all in, a simple and efficient detection method for monitoring food spoilage can not only avoid excessive food waste but also protect the safety of consumers and food safety.

Acknowledgments

We acknowledge the financial support from Fonds National de la Recherche Scientifique (PDR T.0095.21, CDR J.0064.23) and the China Scholarship Council (201804910584, LS). We thank all our collaborators who contributed to this Ph.D. thesis and whose names are cited in our publication list.

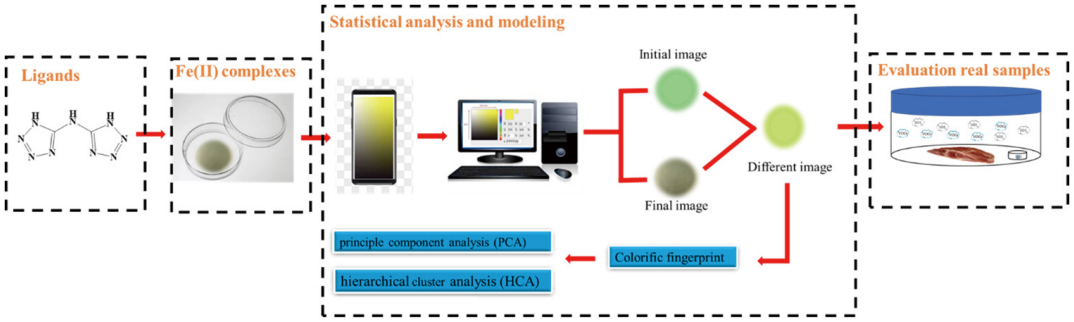

Figure 13. Schematic representation of progress tracking of thesis' objective.

References

[1] Tsai, W. T., An overview of health hazards of volatile organic compounds regulated as indoor air pollutants. *Rev. Environ. Health.* **2019**, *34*, 81-89.

[2] Lamplugh, A.; Harries, M.; Xiang, F.; Trinh, J.; Hecobian, A.; Montoya, L. D., Occupational exposure to volatile organic compounds and health risks in Colorado nail salons. *Environ. Pollut.* **2019**, *249*, 518-526.

[3] Li, D.; Xu, X.; Li, Z.; Wang, T.; Wang, C., Detection methods of ammonia nitrogen in water: A review. *TrAC - Trends Anal. Chem.* **2020**, *127*, 115890.

[4] Woollam, M.; Teli, M.; Angarita-Rivera, P.; Liu, S.; Siegel, A. P.; Yokota, H.; Agarwal, M., Detection of volatile organic compounds (VOCs) in Urine via gas chromatography-mass spectrometry QTOF to differentiate between localized and metastatic models of breast cancer. *Sci. Rep.* **2019**, *9*, 2526.

[5] Kamarulzaman, N. H.; Le-Minh, N.; Stuetz, R. M., Identification of VOCs from natural rubber by different headspace techniques coupled using GC-MS. *Talanta* **2019**, *191*, 535-544.

[6] Mohd Ali, M.; Hashim, N.; Abd Aziz, S.; Lasekan, O., Principles and recent advances in electronic nose for quality inspection of agricultural and food products. *Trends Food Sci. Technol.* **2020**, *99*, 1-10.

[7] Siripongpreda, T.; Siralertmukul, K.; Rodthongkum, N., Colorimetric sensor and LDI-MS detection of biogenic amines in food spoilage based on porous PLA and graphene oxide. *Food Chem.* **2020**, *329*, 127165.

[8] Sun, L., Design of novel colorimetric sensors based on Fe(II) for detection of volatile organic compounds. *UCLouvain doctoral thesis* **2023**.

[9] Sun, L.; Ndiaye, M.; El Islam Belmouri, N.; Robeyns, K.; Rotaru, A.; Boukheddaden, K.; Garcia, Y., Spin crossover coordination polymers with pyridine-Like modification through selective guest Molecules. *Cryst. Growth Des.* **2022**, *22*, 7555-7563.

[10] Sun, L.; Belmouri, N. E. I.; Ndiaye, M.; Robeyns, K.; Rotaru, A.; Boukheddaden, K.; Garcia, Y., Thermal-Driven Guest-Induced Spin Crossover Behavior in 3D Fe(II)-Based Porous Coordination Polymers. *Crystal Growth Des.* **2023**, *23*, 3402-3411.

[11] Sun, L.; Li, X.; Vandenbulcke, C.; Belmouri, N. E. I.; Bouchez, G.; Robeyns, K.; Rotaru, A.; Boukheddaden, K.; Garcia, Y. Stimuli-Responsive Spin Crossover Behavior in 3D Fe(II) Porous Coordination Polymer for Guest Molecules. *Mater. Adv.*, submitted.

[12] Sun, L.; Rotaru, A.; Robeyns, K.; Garcia, Y., A colorimetric sensor for the highly selective, ultra-sensitive, and rapid detection of volatile organic compounds and hazardous gases. *Ind. Eng. Chem. Res.* **2021**, *60*, 8788-8798.

[13] Naik, A. D.; Robeyns, K.; Meunier, C. F.; Léonard, A. F.; Rotaru, A.; Tinant, B.; Filinchuk, Y.; Su, B. L.; Garcia., Y., Selective and reusable iron(II)-based molecular sensor for the vapor-phase detection of alcohols. *Inorg. Chem.* **2014**, *53*, 1263-1265.

[14] Guo, Y.; Xue, S.; Dîrtu, M. M.; Garcia, Y., A versatile iron(II)-based colorimetric sensor for the vapor-phase detection of alcohols and toxic gases. *J. Mater. Chem. C* **2018**, *6*, 3895-3900.

[15] Danielsson, P.-E., Euclidean distance mapping. Comput. Graph. *Image Process.* **1980**, *14*, 227-248.

[16] J. Joe H. Ward, Hierarchical grouping to optimize an objective function. *J. Am. Stat. Assoc.* **1963**, *58*, 236-244.

[17] Lim, S. H.; Feng, L.; Kemling, J. W.; Musto, C. J.; Suslick, K. S., An optoelectronic nose for the detection of toxic gases. *Nat. Chem.* **2009**, *1*, 562-567.

[18] Scott, S. M.; James, D.; Ali, Z., Data analysis for electronic nose systems. *Microchim. Acta* **2006**, *156*, 183-207.

[19] Plaisance, H.; Blondel, A.; Desauziers, V.; Mocho, P., Hierarchical cluster analysis of carbonyl compounds emission profiles from building and furniture materials. *Build. Environ.* **2014**, *75*, 40-45.

[20] Boukheddaden, K.; Ritti, M. H.; Bouchez, G.; Sy, M.; Dîrtu, M. M.; Parlier, M.; Linares, J.; Garcia, Y., Quantitative contact pressure sensor based on spin crossover mechanism for civil security applications. *J. Phys. Chem. C* **2018**, *122*, 7597-7604.

[21] Gütlich, P.; Gaspar, A. B.; Garcia, Y., Spin state switching in iron coordination compounds. *Beilstein J. Org. Chem*. **2013**, *9*, 342-391.

[22] Robert, F.; Naik, A. D.; Tinant, B.; Robiette, R.; Garcia, Y., Insights into the origin of solid-state photochromism and thermochromism of N-salicylidene anils: the intriguing case of aminopyridines. *Chem. Eur. J.* **2009**, *15*, 4327-4342.

[23] Ma, Z.; Chen, P.; Cheng, W.; Yan, K.; Pan, L.; Shi, Y.; Yu, G., Highly sensitive, printable nanostructured conductive polymer wireless sensor for food spoilage detection. *Nano Lett.* **2018**, *18*, 4570–4575.

[24] Nguyen, L. H.; Naficy, S.; McConchie, R.; Dehghani, F.; Chandrawati, R., Polydiacetylene-based sensors to detect food spoilage at low temperatures. *J. Mater. Chem. C* **2019**, *7*, 1919-1926.

[25] Mohammadi, Z.; Jafari, S. M., Detection of food spoilage and adulteration by novel nanomaterial-based sensors. *Adv. Colloid. Interface Sci.* **2020**, *286*, 102297.

[26] Sun, L.; Rotaru, A.; Garcia, Y., A non-porous Fe(II) complex for the colorimetric detection of hazardous gases and the monitoring of meat freshness. *J. Hazard. Mater.* **2022**, *437*, 129364.

[27] Li, W.; Sun, L.; Liu, C.; Rotaru, A.; Robeyns, K.; Singleton, M. L.; Garcia, Y. Supramolecular Fe(II)4L4 cage for fast ammonia sensing. *J. Mater. Chem. C* **2022**, *10*, 9216 - 9221. **Hot paper**. Inside **Front cover**.

Future Conferences, Symposia, Workshops

May 27 -31, 2024
Mössbauer Spectroscopy in Materials Science (MSMS 2024)
Kurdějov, Czech Republic
http://cssc2024.spektroskopie.cz/

September 1 - 5, 2024
International Symposium on the Industrial Applications of the Mössbauer Effect (ISIAME 2024)
Fukuoka, Japan
https://www.omenscilab.org/isiame2024/

Center for Advanced Mössbauer Spectroscopy

Dalian Institute of Chemical Physics, Chinese Academy of Sciences

is pleased to offer these services of the Mössbauer spectra (MS) measurement & analysis to the international community. Your any special request will be carefully considered.

We offer

- Room temperature ^{57}Fe/ ^{119}Sn MS
- Room temperature ^{57}Fe / ^{119}Sn CEMS
- Low temperature transmission ^{57}Fe MS
- Frozen solution ^{57}Fe MS
- Electrochemical in-situ/operando ^{57}Fe / ^{119}Sn MS
- Ion battery in-situ/operando ^{57}Fe / ^{119}Sn MS
- Photocatalytic in-situ/operando ^{119}Sn MS
- Photoelectrocatalytic in-situ/operando ^{57}Fe / ^{119}Sn MS
- Temperature, pressure and atmosphere control in-situ/operando ^{57}Fe / ^{119}Sn MS

Contact

Email: mossbauer@dicp.ac.cn

Phone: +86-411-84379711

Center for Advanced Mössbauer Spectroscopy
Dalian Institute of Chemical Physics
Chinese Academy of Sciences
457 Zhongshan Road, Dalian 116023, China

http://wangjh.dicp.ac.cn/csfw.htm
http://wangjh.dicp.ac.cn/English/Services.htm

RITVERC
Isotopenprodukte

#Co-57
#Sn-119m
#Fe-57 reference absorbers
#Source grippers

Since 2023 → a new distributor in North and South America:
ISOFLEX Radioactive LLC, iso-rad.com, +1 (415) 440-4433

ritverc.com